Single-cell RNA profiling of *Plasmodium vivax*-infected hepatocytes reveals parasite- and host- specific transcriptomic signatures and therapeutic targets

Anthony A Ruberto [a], Steven P Maher [a], Amélie Vantaux [b], Chester J Joyner [a,c], Caitlin Bourke [d,e], Balu Balan [d,f] , Aaron Jex [d,e,f], Ivo Mueller [d,e] , Benoit Witkowski [b], Dennis E Kyle [a]

[a] Center for Tropical and Emerging Global Diseases, University of Georgia, Athens, GA, United States

[b] Malaria Molecular Epidemiology Unit, Institut Pasteur du Cambodge, Phnom Penh, Cambodia

[c] Department of Infectious Diseases, College of Veterinary Medicine, University of Georgia, Athens, GA, USA

[d] Population Health & Immunity Division, Walter and Eliza Hall Institute, Parkville, Victoria, Australia

[e]Department of Medical Biology, The University of Melbourne, Parkville, Victoria, Australia

[f] Faculty of Veterinary and Agricultural Sciences, University of Melbourne, Parkville, Victoria, Australia

Running Head: single-cell RNA-seq of *P. vivax*-infected hepatocytes

Address correspondence to dennis.kyle@uga.edu

ABSTRACT

The resilience of *Plasmodium vivax*, the most widely distributed malaria-causing parasite in humans, is attributed to its ability to produce dormant liver forms known as hypnozoites, which can activate weeks, months, or even years after an initial mosquito bite. The factors underlying hypnozoite formation and activation are poorly understood, as is the parasite's influence on the host hepatocyte. Here, we shed light on transcriptome-wide signatures of both the parasite and the infected host cell by sequencing over 1,000 *P. vivax*-infected hepatocytes at single-cell resolution. We distinguish between replicating schizonts and hypnozoites at the transcriptional level, identifying key differences in transcripts encoding for RNA-binding proteins associated with cell fate. In infected hepatocytes, we show that genes associated with energy metabolism and antioxidant stress response were upregulated, and those involved in the host immune response downregulated, suggesting both schizonts and hypnozoites alter the host intracellular environment. The transcriptional markers in schizonts, hypnozoites, and infected hepatocytes revealed here pinpoint potential factors underlying dormancy and can inform therapeutic targets against *P. vivax* liver-stage infection.

INTRODUCTION

Malaria is a significant global health burden, with an estimated 421 million cases and 627,000 deaths per year (World Health Organization, 2021). At least five *Plasmodium* species are known to infect humans, with *P. vivax* responsible for the majority of cases outside Africa (World Health Organization, 2021). All *Plasmodium* parasites that infect humans have an obligatory developmental stage in the liver where the parasite undergoes asexual reproduction known as schizogony within a hepatocyte before releasing thousands of merozoites into the blood. In *P. vivax*, a proportion of parasites known as hypnozoites forgo immediate division in hepatocytes, and persist in the liver for weeks, months, or years before activating to initiate schizogony resulting in a relapse blood infection (Adams and Mueller, 2017; Krotoski et al., 1982). Hypnozoites are thought to cause up to 90% of cases in certain geographical regions (Adekunle et al., 2015; Commons et al., 2020; Robinson et al., 2015), and mathematical models predict that eliminating *P. vivax* malaria will be difficult without interventions that target hypnozoite reservoirs (White et al., 2018).

The factors influencing the biogenesis, persistence, and activation of hypnozoites are poorly understood. Studies have found that hypnozoites in temperate versus tropical regions have long and short latencies, respectively, suggesting a correlation between geographical region and relapse patterns (Battle et al., 2014; Huldén et al., 2008; Krotoski et al., 1986; White, 2011). These findings suggest the developmental trajectory is genetically encoded, and support the hypothesis that it is somehow pre-programmed in the sporozoite (Lysenko et al., 1977; Ungureanu et al., 1976); but other contributing

factors from the host could play a role in determining whether the sporozoite becomes a schizont or hypnozoite (Schäfer et al., 2021).

Our understanding of *P. vivax* liver stage biology at the cellular and molecular level is in its nascency for two overarching reasons. First, protocols to cryopreserve and continuously maintain erythrocytic stage parasites *in vitro* are lacking, necessitating the collection of gametocyte-infected blood from human volunteers in *P. vivax* malaria-endemic regions to generate the sporozoites required to initiate an infection. New laboratory models have recently been developed which can partially alleviate the need to obtain gametocytes from human-infected blood (Mikolajczak et al., 2015; Schäfer et al., 2020), yet these sources are expensive and each have distinct logistical hurldes. In addition to the sporozoite limitation, upon initiating a *P.* vivax-infected hepatocyte culture, the high ratio of noninfected versus infected hepatocytes has historically made it difficult to isolate and study these forms in sufficient numbers. Robust *in vitro* pre-erythrocytic platforms capable of long-term culture of sufficient numbers of *P. vivax* liver stages have only recently been developed (Maher et al., 2021; Roth, Maher et al., 2018). For these reasons, much of our knowledge of hypnozoite biology at the molecular level remains limited to studies using *P. cynomolgi*—a parasite capable of causing relapsing infections in non-human primates for which molecular tools are available (Chua et al., 2019; Cubi et al., 2017; Voorberg-van der Wel et al., 2017, 2020). However, it is unknown whether mechanisms regulating hypnozoite formation and dormancy are consistent across the different relapsing malaria parasites.

Transcriptome-wide profiling of *P. vivax* liver stages has previously been performed using a bulk RNA sequencing strategy (Gural et al., 2018). While informative, the data provide insights only into average transcript levels derived from either mixed (schizont and hypnozoite) or hypnozoite-only populations, masking any transcriptional variation that might exist between individual parasites. Second, the parasite's potential impact on the hepatocyte is not considered, barring analysis of host-pathogen interactions. Nevertheless, these shortcomings highlight a need to better understand differences between individual parasites, as well as how the parasite alters the hepatocyte. Advancements in these areas could help elucidate parasite- and host-factors important for the parasite's liver stage development.

Single-cell RNA-sequencing (scRNA-seq) methods offer new ways of studying cell-to-cell variation (Aldridge and Teichmann, 2020), and have already allowed for novel insights into host-pathogen interactions in various disease contexts (Penaranda and Hung, 2019). In *Plasmodium* spp., scRNA-seq analyses have so far revealed that individual parasite forms exist on a spectrum of transcriptomic states (Bogale et al., 2021; Howick et al., 2019; Poran et al., 2017; Real et al., 2021; Reid et al., 2018; Ruberto et al., 2021a), and applying them to study the biology of *P. vivax* is a burgeoning area of research (Mancio-Silva et al., 2022; Ruberto et al., 2021b; Sà et al., 2020). Droplet-based techniques, such as 10x Genomics' gene expression platform (Zheng et al., 2017), allow for the

84 sequencing of several thousands of cells, increasing the chances of observing rare cell populations (e.g.
85 hepatocytes infected with *P. vivax*). We therefore presumed that applying scRNA-seq to *P. vivax* liver
86 forms derived using an *in vitro* platform would prove a fruitful avenue of inquiry into the parasite's
87 biology at the transcription level.

88 Using scRNA-seq, we characterize transcriptomic signatures of parasite and host in an *in vitro*
89 *P. vivax* liver stage model. We find differences in gene expression between replicating schizonts and
90 hypnozoites, and reveal variation, previously unobservable by bulk sequencing approaches, between
91 individual hypnozoites. In infected hepatocytes, we find that genes associated with energy metabolism
92 and antioxidant stress response are upregulated, and those involved in the host immune response
93 downregulated. Various host genes associated with these processes are found to be exclusively
94 upregulated during hypnozoite infection. Our study elucidates the transcriptional signatures among
95 infected hepatocytes and presents potential mechanisms *P. vivax* can use to either exploit its host for
96 rapid proliferation or to quietly persist, remaining undetected by the host immune system.

97 **RESULTS**

98 **Strategy used to study *P. vivax* liver stage biology**

99 Primary human hepatocytes were cultured and infected with *P. vivax* sporozoites on a 384-well plate
100 platform (Maher et al., 2021; Roth, Maher et al., 2018). **Figure 1A** outlines the workflow for the
101 experiment. Following infection with sporozoites, cultures were assessed at two endpoints: one
102 containing both schizonts and hypnozoites at day 5 post-infection, and the other containing solely
103 hypnozoites at day 9 post-infection. Schizonts were eliminated from day 9 post-infection cultures by
104 adding the phosphatidylinositol 4-kinase (PI4K) inhibitor MMV390048 (1 μM) to the culture media on
105 days 5, 6 and 7 post-infection (Gural et al., 2018; Paquet et al., 2017). For each collection time point,
106 we simultaneously initiated two sets of hepatocyte cultures: one infected with sporozoites for
107 quantification of immunofluorescent-labeled parasites by high-content imaging (HCI), and one infected
108 with sporozoites for transcriptional profiling using a high-throughput, droplet-based scRNA-seq
109 workflow (Zheng et al., 2017). As controls, a third set of naïve cultures were left uninfected and
110 processed for scRNA-seq alongside cultures at days 5 and day 9 post-infection. At each collection point,
111 a target of approximately 10,000 individual hepatocytes were partitioned into droplets prior to the
112 generation of RNA libraries. Droplets contained primers with unique nucleotide sequences (cellular
113 barcodes) that were incorporated into the transcript sequence during the reverse transcription step,
114 allowing for the identification of each transcript's cellular origin. After sequencing the single-cell
115 libraries, we mapped the resulting reads onto a customized reference transcriptome containing human
116 (Ensembl, v103) and *P. vivax* PVP01 (PlasmoDB, v51) information. The *P. vivax* PVP01 transcript

117 information included the nucleotides encoding for the gene-flanking untranslated regions (UTRs)
118 (Siegel, Chappell et al., 2020), which is important because of the poly-dT capture strategy of the
119 technology used in our workflow. This information partially alleviates the challenges associated with
120 transcription quantification (Ruberto et al., 2021b; Sà et al., 2020). Post mapping, we used the transcript
121 information (i.e. human or parasite encoding) with their designated cellular barcodes to assess the
122 number of transcripts in each cell, and to determine which hepatocytes were infected.

123 As expected, we detected hepatocytes infected with either form of the parasite at 5 days post-
124 infection, and only hypnozoites at 9 days post-infection following exposure to MMV390048 (**Figure**
125 **1B and Figure 1—figure supplement 1**). Visual assessment of infected cultures fixed and stained with
126 an antibody against Upregulated in Infectious Sporozoites 4 (*Pv*UIS4), which localizes to the parasite's
127 parasitophorous vacuole membrane, confirmed that the parasites we subjected to scRNA-seq had
128 properly invaded hepatocytes and initiated development into hypnozoites and schizonts. Furthemore,
129 hypnozoites displayed typical morphology relative to those found in humanized mice (Mikolajczak et
130 al., 2015) and *in vitro* (Roth, Maher et al., 2018). **Figure 1C** displays the distribution of individual
131 parasite growth areas, number of parasites detected, and parasitemia levels at each endpoint. Across
132 replicates, the parasitemia ranged from 5.50-6.93% at 5 days post-infection and 1.76-2.77% at 9 days
133 post-infection. Together, the high infection rates coupled with the high-throughput capacity of 10x
134 Genomics' single-cell isolation and sequencing workflow allowed for sufficient material to be generated
135 for successful profiling of both parasite and host transcriptomes.

136 ***P. vivax* schizonts and hypnozoites are distinguishable at single-cell resolution**

137 We first analyzed the reads mapping to *P. vivax* transcripts to identify schizonts and hypnozoites, as
138 well as to assess the extent to which these forms differed at single-cell resolution. In total, we
139 characterized 1,438 parasite transcriptomes across two independent experimental replicates (**Figure 2—**
140 **figure supplement 1A**). The number of parasite transcriptomes profiled corroborated the parasitemia
141 levels quantified using high-content imaging. This correlative evidence suggests that our cell and gene
142 filtering cutoffs effectively eliminated problematic cells (i.e. poorly captured, dying, or dead) (**Figure**
143 **2—figure supplement 1B and Figure 2—source data 1**). Low dimensional representation of the data
144 revealed two populations of parasites in samples profiled at 5 days post-infection (**Figure 2A, left**). In
145 contrast, and as expected, samples profiled at 9 days post-infection contained one population (**Figure**
146 **2A, right**). Given that the population of cells profiled at day 9 post-infection, from which schizonts were
147 chemically removed, overlapped with one of the two cell populations profiled at 5 days post-infection,
148 we deduced that the non-overlapping population of cells encoded for schizonts. Consistent with our
149 reasoning, an unsupervised clustering algorithm (Traag et al., 2019) unbiasedly assigned the cells to one
150 of the two clusters (**Figure 2B and Figure 2—figure supplement 1C**). As expected, the number of

151 transcripts detected, the unique molecular identifier (UMI) counts (a readout for absolute transcript
152 abundances (Kivioja et al., 2011)), and the transcript levels of the early liver stage development marker
153 liver stage-specific protein, LISP2 (PVP01_0304700) (Gupta et al., 2019), all displayed greater
154 quantities in the schizont cluster (C2) relative to the hypnozoite cluster (C1) (**Figure 2C**).

155 Previous scRNA-seq studies in *Plasmodium* spp. has shown gene expression varies with life-
156 cycle stage, with non-replicating forms displaying less expression per cell compared to replicating forms
157 (Howick et al., 2019). The median number of genes detected in schizonts (2323) was greater than the
158 values observed in other single-cell assessments of replicating stages of the parasite's life cycle (**Figure**
159 **2—figure supplement 2**) (Mancio-Silva et al., 2022; Sà et al., 2020). Furthermore, the median number
160 of UMIs per schizont (6905) was also greater in the current dataset versus other reports. The median
161 number of genes detected per hypnozoite (519) and median number of UMIs per hypnozoite (672) were
162 consistent with other single-cell reports assessing non-replicating, uninucleate stages (Bogale et al.,
163 2021; Real et al., 2021; Ruberto et al., 2021a), including recent single-cell assessments of *P. vivax*
164 sporozoites (Ruberto et al., 2021b) and hypnozoites (Mancio-Silva et al., 2022) (**Figure 2—figure**
165 **supplement 2**). The intact parasitophorous vacuole membrane of hypnozoites in cultures assessed on
166 days 5 and 9 (**Figure 1B and Figure 1—figure supplement 1**), the association between infection rates
167 observed by IFA and the number of transcriptomes assessed, and the per cell metrics typical of
168 *Plasmodium* spp. life stages with low RNA content cells together provided us with strong assurance that
169 the transcriptomes obtained represented viable hypnozoites. These findings show that the transcriptomes
170 of *P. vivax* schizonts and hypnozoites can be distinguished using our experimental workflow.

171 **Hypnozoites exhibit distinct transcriptional signatures compared to schizonts**

172 We next performed differential gene expression analysis to identify transcriptome-wide differences
173 distinguishing schizonts and hypnozoites. Using stringent inclusion cutoffs (Bonferroni adjusted p value
174 < 0.01 & absolute (average $\log_2$ fold change [FC]) > 0.5), we found significant differences in the
175 expression of ~18% (836/4722) of genes detected (**Figure 3—figure supplement 1A; Figure 3—**
176 **source data 1A**). Relative to hypnozoites, we found an increase in the expression levels of 368 genes
177 in schizonts. As expected, we observed a significant increase of LISP2 gene expression in schizonts
178 (average $\log_2$ FC: 2.32) compared to hypnozoites. Shortly after invading the hepatocyte, non-relapsing
179 *Plasmodium* spp. liver forms undergo immediate replication. Studies in rodent malaria models have
180 shown that these forms are metabolically active and that various genes involved in energy metabolism
181 are upregulated (Caldelari et al., 2019; Tarun et al., 2008; Toro-Moreno et al., 2020). Consistent with
182 these prior observations, we found an increased transcription associated with glycolysis
183 (PVP01_0816000, PVP01_1229700, PVP01_1244000) and the TCA cycle (PVP01_0106100,
184 PVP01_1332400) in schizonts (**Figure 3—figure supplement 1B; Figure 3—source data 1A**). More

185 broadly, we found increased transcription of various metabolic processes, as well as motility, DNA-,
186 RNA-, and protein-processing (**Figure 3—figure supplement 1C; Figure 3—source data 1A**). Genes
187 encoding for various proteasome subunits displayed greater transcription in schizonts (**Figure 3—figure**
188 **supplement 2A; Figure 3—source data 1A**). To further show the importance of this protein complex,
189 we tested a known proteosome inhibitor, carfilzomib (Kortuem and Stewart, 2013), in our standard 12-
190 day *P. vivax* small molecule screening assay (Maher et al., 2021), and found it effectively killed
191 schizonts (IC_{50} 288nM) and hypnozoites (IC_{50} 511nM) with some selectivity over host hepatocytes (IC_{50}
192 3.32 μM) (**Figure 3—figure supplement 2C and D**).

193 The detection of genes associated with energy metabolism in hypnozoites, albeit at lower levels
194 relative to schizonts, suggested that these forms are also metabolically active (**Figure 3—figure**
195 **supplement 1B**). Relative to schizonts, we found an increase in expression of 468 genes in hypnozoites
196 (**Figure 3—source data 1A**). As represented in **Figure 3A**, genes with greater expression in
197 hypnozoites encoded for a diverse set of ontologies—including proteases, membrane proteins,
198 transcription factors, and DNA-/RNA-regulating proteins. Genes encoding for proteases vivapain-1,
199 vivapain-2 (PVP01_1248900, PVP01_0916200), and plasmepsin IV (PVP01_1340900) displayed the
200 greatest differential expression in these forms compared to schizonts (**Figure 3A and B; Figure 3—**
201 **source data 1A**). While limited research has reported the functionality of these gene products in *P.*
202 *vivax* (Byoung-Kuk et al., 2004), work in other *Plasmodium* spp. has revealed that they localize to the
203 food vacuole and play an important role in hemoglobin catabolism during the blood stages of the
204 parasite's life cycle (Dame et al., 2003; Drew et al., 2008).

205 We also identified genes with greater expression associated with RNA regulatory mechanisms
206 in hypnozoites. Notably, we found greater expression of CCR4 (PVP01_1429000), a gene encoding for
207 a protein with mRNA deadenylase activity and playing a role in mRNA turnover (Tucker et al., 2001)
208 (**Figure 3—source data 1A**). In *Plasmodium* spp., it has been described as important in regulating the
209 expression of genes associated with invasion and egress in blood stages (Balu et al., 2011). RNA-binding
210 proteins (RBPs) also govern gene expression at the post-transcriptional level by transiently storing
211 transcripts until later processing (Hentze et al., 2018). Pumilio domain (PUF) proteins are a major family
212 of RBPs that regulate cellular fating through translational repression in eukaryotes. We found greater
213 expression of the gene encoding for PUF1 (PVP01_1015200) in hypnozoites relative to schizonts
214 (**Figure 3A and B**; **Figure 3—source data 1A**). Furthermore, we found greater expression of 7-Helix-
215 1 protein (PVP01_1008400) (**Figure 3A and B**; **Figure 3—source data 1A**)—a stress granule
216 component that interacts with the RNA-binding protein PUF2 and serves to be crucial for protein
217 synthesis in *P. falciparum* (Miao et al., 2010). Numerous studies have shown that *Plasmodium* spp. use
218 various post-transcriptional regulatory mechanisms to coordinate stage transitions and development
219 (Baumgarten et al., 2019; Bunnik et al., 2016; Foth et al., 2011; le Roch et al., 2004; Tarun et al., 2008;

220 Vembar et al., 2016). Our data corroborate these findings and suggest that similar strategies may be used
221 in *P. vivax* to regulate liver stage development. Moreover, these data suggest that RBP-mediated cellular
222 fating and translational repression may be involved in regulating hypnozoite quiescence.

223 Given the potential role in RBP-mediated cellular fating and translational repression governing
224 hypnozoite quiescence, we performed further analyses focused on RBP-mediated regulation. To this
225 end, we scanned the *P. vivax* genome searching for genes encoding for cellular fating RBPs based on
226 ortholog groups (OGs) of known human cellular fating RBPs (348 RBPs; 227 OGs), identifying 89 OGs
227 (99 RBPs) in *P. vivax.* We detected 48 genes encoding for cellular fating RBPs with greater expression
228 in schizonts (**Figure 3C, left**; **Figure 3—source data 1B**). Notably, we identified eukaryotic
229 translational initiation factors (PVP01_1238100, PVP01_0531200, PVP01_1431600, PVP01_0807600,
230 PVP01_1005600, PVP01_0519700, PVP01_1329200, PVP01_0825000, PVP01_1303500), and
231 splicing factors (PVP01_0716000, PVP01_0521000, PVP01_0804100, PVP01_1111800,
232 PVP01_0607600, PVP01_1012200) suggesting active translational events. Gene Ontology (GO) term
233 analysis revealed that these transcripts were associated with translation initiation (GO:0005852;
234 GO:0033290; GO:0016282) (adjusted p value < 0.05, **Figure 3C, right**; **Figure 3—source data 1C**).

235 In hypnozoites, we detected 51 genes encoding for cellular fating RBPs with increased
236 expression relative to schizonts (**Figure 3C, left**; **Figure 3—source data 1B**). These genes encode for
237 prominent P body markers, namely DOZI/DDX6 (PVP01_0819400), CCR4-NOT complex proteins
238 (PVP01_1429000, PVP01_1014400, PVP01_1331700, PVP01_1453400, PVP01_0929400), mRNA-
239 decapping enzyme subunit 1 (PVP01_0617200), mRNA-decapping enzyme subunit 2
240 (PVP01_1409900), UPF1 (PVP01_0805200), UPF2 (PVP01_0724300), UPF3 (PVP01_1226700),
241 PUF2 (PVP01_0526500), PABP (PVP01_1442500), Fibrillarin (PVP01_1341600) and trailer hitch
242 homolog (PVP01_1269800) (**Figure 3—source data 1B**). Genes encoding for cellular fating RBPs in
243 hypnozoite also represented GO terms corresponding to active biological condensate formations, such
244 as the CCR4-NOT complex (GO:0030014; GO:0030015) and the P body (GO:0000932) (adjusted p
245 value < 0.05, **Figure 3C, right; Figure 3—source data 1C**). Together, these findings suggest that P
246 body-mediated cell fating could be important in regulating hypnozoite persistence.

247 **Transcriptomic heterogeneity exists amongst individual *P. vivax* hypnozoites**

248 Having described the transcriptomic signatures distinguishing schizonts and hypnozoites, we next
249 sought to assess the extent to which gene expression varied amongst hypnozoites. We thus parsed the
250 data into only hypnozoite transcriptomes. In total, 1,147 transcriptomes were assessed (**Figure 4A, left**).
251 Low dimensional representation of the data revealed slight variation between samples collected at days
252 5 and 9 post-infection (**Figure 4A, right**). After regrouping the data using the same unsupervised

253 clustering algorithm described previously, we identified three clusters (**Figure 4B, right**). The
254 proportion of hypnozoites in each cluster varied across the day of collection: specifically, the proportion
255 of hypnozoites in cluster 3 (C3) was greater in hypnozoites collected at day 9 compared to day 5 post-
256 infection (**Figure 4B, left; Figure 4—figure supplement 1A**). Albeit lower compared to schizonts, we
257 also observed a trend for slightly greater gene expression of LISP2 in C3 relative to the other two clusters
258 (**Figure 4C**).

259 We next identified markers that define the hypnozoites in each cluster using the FindAllMarkers
260 function in Seurat (Stuart et al., 2019). We defined a marker as a gene displaying greater than 0.5 FC
261 (average $\log_2$) compared to the other clusters. In total, we detected 477 markers (Bonferroni adjusted p
262 value < 0.05) (**Figure 4—figure supplement 1B**; **Figure 4—source data 1A**). Notable markers in C1
263 included genes associated with drug resistance (PVP01_1447300, PVP01_1259100, and
264 PVP01_1010900), energy metabolism (PVP01_1435000 and PVP01_1122800), protein modification
265 (PVP01_1248900 and PVP01_0916200), and RNA-binding proteins (PVP01_0939900 and
266 PVP01_0819400); in C2, genes associated with translation (PVP01_1255500 and PVP01_0822500);
267 and in C3, genes associated with translation (PVP01_0213700 and PVP01_0203400), fatty acid
268 metabolism (PVP01_1143000 and PVP01_1022800), protein processing (PVP01_1308000 and
269 PVP01_0927700) and ion transport (PVP01_1407500) (**Figure 4D**; **Figure 4—source data 1A**).

270 We next explored the data in the context of cellular fating to elucidate potential patterns in RBP
271 signatures. Among the hypnozoite markers found within our sub-clustering analysis, we identified 80
272 cellular fating RBPs (**Figure 4E, top; Figure 4—source data 1B**). Approximately 4% (3/80) of the
273 differentially expressed genes in C3 encoded for genes associated with cellular fating. In this cluster,
274 the increased gene expression of eukaryotic translation initiation factor 4E (PVP01_0203400) further
275 suggests active translation events may be occurring. C2 contained 20% (16/80) of the cellular fating
276 RBPs differentially expressed. In this cluster, we found RBPs which are important determinants of cell
277 proliferation from a state of quiescence such as eukaryotic translation initiation factor 5A
278 (PVP01_1303500), polypyrimidine tract binding protein (PVP01_1142400), GTP-binding nuclear
279 protein RAN/TC4 (PVP01_0918300), and transformer-2 protein homolog beta (PVP01_0802200). C1
280 contained the majority of the differentially expressed genes encoding for RBPs (~76%, 61/80). Within
281 this cluster, we identified prominent P body markers with cellular fating ability, such as DOZI/DDX6
282 (PVP01_0819400), CCR4-NOT complex proteins (PVP01_1429000, PVP01_1014400,
283 PVP01_1331700, PVP01_1453400), UPF1 (PVP01_0805200), UPF2 (PVP01_0724300), PABP
284 (PVP01_1442500), Fibrillarin (PVP01_1341600) and trailer hitch homolog (PVP01_1269800). GO
285 analysis revealed enrichment of cellular compartments associated to biological condensate formations,
286 namely CCR4-NOT complex (GO:0030014), P granule (GO:0043186), and germplasm (GO:0060293)
287 (**Figure 4E, bottom; Figure 4—source data 1C**).

288 These findings, combined with the shift of hypnozoite proportions and increasing level of *LISP2*
289 from C1 to C3, allowed us to infer the phenotype of hypnozoites in these clusters. As these observations
290 likely represent populations of hypnozoites in persisting and activating states, we defined clusters C1,
291 C2, and C3 to represent persisting, early activating, and late activating hypnozoites, respectively.
292 Together, these findings further our understanding of *P. vivax* hypnozoites through characterization of
293 gene usage and putative regulatory mechanisms in activating and persister forms. Furthermore, they
294 highlight a potential role of P body-mediated cellular fating governing persister hypnozoites.

295 **Strategy used to assess hepatocytes infected with *P. vivax* parasites**

296 After deciphering the identities of *P. vivax* transcriptomes representing schizonts and hypnozoites, we
297 next sought to characterize the transcriptional signatures of hepatocytes infected with either of these
298 forms. To this end, we integrated the data across all the conditions (**Figure 5—supplement 1A and B)**
299 and examined whether distinct sub-populations of infected hepatocytes existed. As highlighted by the
300 low dimensional visualization of the data, we did not find a prominent pattern of infection (**Figure 5**).
301 Moreover, we detected parasites in hepatocytes with different metabolic states (MacParland et al., 2018),
302 as represented by their transcriptional signatures associated with different hepatocyte zonation programs
303 (**Figure 5—supplement 1C and D**).

304 **Identification of transcriptional signatures in *P. vivax*-infected hepatocytes**

305 To identify host transcriptional signatures specific to infection status, we performed differential gene
306 expression analysis, comparing infected to non-infected hepatocytes. Among the hepatocytes infected
307 with schizonts, 106 genes displayed greater expression and 16 displayed decreased expression **(Figure**
308 **6—source data 1A)**; while in hepatocytes infected with hypnozoites, 365 genes displayed greater
309 expression and 41 genes displayed decreased expression (**Figure 6—source data 1B**) (Bonferroni
310 adjusted p value < 0.05). As depicted in the volcano plots in **Figure 6A**, the magnitude of change in
311 expression in the infected versus non-infected cells (average $\log_2$ fold change) was greater in hepatocytes
312 containing schizonts compared to those containing hypnozoites.

313 To gain greater insights into the biological processes and pathways that characterize a schizont-
314 or hypnozoite-infected hepatocyte, we performed enrichment analysis (Raudvere et al., 2019)—scoring
315 18,594 gene sets against the genes differentially expressed in each of our transcriptional comparisons.
316 When considering both the schizont- and hypnozoite-infected hepatocyte populations, we detected a
317 total of 254 enriched gene sets (Bonferroni adjusted p value < 0.05) (**Figure 6B**; **Figure 6—source data**
318 **1C**). Approximately 18% (45/254) of these gene sets overlapped in hepatocytes infected with either
319 schizonts or hypnozoites (**Figure 6—source data 1D**). These data indicate that while some overlap

320 exists in the gene networks the parasite alters during infection, the majority of processes and pathways
321 altered are specific to schizont versus hypnozoite infected hepatocytes.

322 Using these gene sets, we then constructed network enrichment maps (Merico et al., 2010) to
323 provide a global overview of the prominent biological themes associated with each infection condition
324 (**Figure 6C and D**). We detected upregulation of genes associated with pathways related to energy
325 metabolism (oxidative phosphorylation, mitochondrial function, and lipid catabolism) in schizont- and
326 hypnozoite-infected hepatocytes. Analysis of the most differentially expressed genes associated with
327 these pathways included *MT-ND2*, *CHCHD10*, and *AKR1B10* (**Figure 6—source data 1A and B**).
328 Corroborating our transcriptomic data , we found an increase in protein levels of AKR1B10 in infected
329 versus non-infected hepatocytes by IFA (**Figure 6E; Figure 6—figure supplement 1**). AKR1B10 has
330 been implicated in cell survival through its regulation of lipid metabolism and elimination of carbonyls
331 (Martin and Maser, 2009; Qu et al., 2021; Wang et al., 2009) and has primarily been described as a
332 biomarker of cancer (Díez-Dacal et al., 2011; Fukumoto et al., 2005; Jin et al., 2006). More recently, it
333 has been shown that its expression is positively correlated with non-alcoholic fatty liver disease
334 (Govaere et al., 2020). In schizonts, the upregulation of genes linked to fatty acid metabolism is
335 consistent with observations in hepatocytes harboring developing forms from non-relapsing
336 *Plasmodium* spp. (Albuquerque et al., 2009; Itoe et al., 2014). We now reveal that infection with
337 hypnozoites also elicits enrichment of genes associated with fatty acid metabolism (**Figure 6D**),
338 suggesting that these forms may be scavenging host resources to fuel their persistence.

339 Previous work assessing *Plasmodium* liver stage biology has revealed that the host is able to
340 detect the parasite (Liehl and Mota, 2012) and that type I interferon plays an integral role in this response
341 (Liehl et al., 2013; Miller et al., 2014). The decrease in expression of genes associated with interferon
342 signaling (REAC:R-HSA-913531, GO:0034340, GO:0034341, GO:0071357, GO:0060337) in
343 hepatocytes infected with either schizonts or hypnozoites suggest that *P. vivax* manipulates the
344 hepatocytes to evade detection (**Figure 6C and D; Figure 6—source data 1C and D**). Furthermore,
345 we found that relative to naïve hepatocytes, uninfected hepatocytes in cultures exposed to *P. vivax*
346 displayed significant downregulation of pathways associated with immune effectors (GO: 0030449,
347 GO:0002697, REAC: R-HSA-166658, R-HSA-168249) (**Figure 6—source data 1E and F**).

348 In hepatocytes infected with schizonts, we found a decrease in expression of NFKB-regulated
349 genes (*SOD2, TMEM45A, CCL20,* and *TPM1*) (**Figure 6—source data 1A**), consistent with findings
350 that *Plasmodium* spp. release signals to block proinflammatory response (Singh et al., 2007). These
351 findings, in addition to the decrease in the expression of *HLA-B*—a molecule involved in antigen
352 presentation to T cells that can trigger their activation when 'self' peptides are not presented—and the
353 neutrophil chemoattractant *CXCL8* suggest that replicating parasites alter hepatocyte signaling pathways

354 to minimize recruitment of innate immune cells and avoid detection by T cells. Similar to hepatocytes
355 infected with schizonts, we found genes associated with interferon signaling downregulated in
356 hepatocytes infected with hypnozoites, namely: *UBB, UBC, HSP90AB1, IFITM3, IFITM2,* and *HLA-A*
357 (**Figure 6—source data 1B**). Furthermore, transcripts associated with the downregulation of class I
358 major histocompatibility complex (*CD81* and *B2M*) were also decreased in these hepatocytes (**Figure**
359 **6—source data 1B**). Together, these findings suggest that *P. vivax* infection of hepatocytes may
360 suppress the secretion of various chemokines and proinflammatory cytokines to thwart the recruitment
361 of inflammatory cells to the site of infection while simultaneously downregulating MHC- I to reduce
362 the chances they will be detected if these cells are successfully recruited.

363 Enrichment analysis linking the changes in gene expression in infected hepatocytes with
364 transcriptional factors revealed distinct sets of putative transcriptional regulators. In total, we detected
365 35 transcription factors with potential roles in governing the gene expression changes in infected
366 hepatocytes (adjusted p value < 0. 05, **Figure 7; Figure 7—source data 1**). In infected hepatocytes, we
367 found enrichment of transcripts governed by NRF2 (**Figure 7; Figure 7—source data 1)**. The
368 regulation of gene expression through NRF2 in infected hepatocytes may serve to minimize reactive
369 oxygen species in the cell (Hayes and Dinkova-Kostova, 2014). Thus, in addition to the decreased
370 expression of genes associated with inflammatory response (**Figure 6—source data 1C**), NRF2-
371 mediated regulation of antioxidant responsive genes may protect hepatocytes from *Plasmodium*-induced
372 stress and thus serve as a complementary means of minimizing the host inflammatory response.

373 **DISCUSSION**

374 The infection of the liver by *P. vivax* constitutes an obligatory step in its life-cycle. *In vivo* studies have
375 shown that within hepatocytes, *P. vivax* can exist in one of two phenotypically-distinct forms: schizonts
376 or hypnozoites (Cogswell, 1992; Mikolajczak et al., 2015). They have also been observed *ex vivo* by
377 infection of hepatocyte monolayers (Gural et al., 2018; Hollingdale et al., 1985; Roth, Maher et al.,
378 2018; Sattabongkot et al., 2006). A key problem hindering the study of *P. vivax* liver stage biology is
379 the difficulty involved in obtaining a sufficient number of infected hepatocytes to make meaningful
380 comparisons between them. We show that by coupling our *in vitro* liver stage model (Maher et al., 2021;
381 Roth, Maher et al., 2018) with a high-throughput single-cell capture technology (Klein et al., 2015;
382 Macosko et al., 2015; Zheng et al., 2017) that transcriptome-wide characterization of *P.* vivax-infected
383 hepatocytes is feasible. The findings provide much needed insight into the molecular signatures of *P.*
384 *vivax* hypnozoites and the host cells they infect.

385 Our work corroborates the growing number of *Plasmodium* spp. scRNA-seq data sets, revealing
386 highly variable gene expression patterns across, and within, the various stages of the parasite's life cycle.

387 Smaller and non-replicating parasites stages (i.e. rings, sporozoites) tend to have fewer genes detected
388 using single-cell approaches. Here, the number of genes detected, as well as the UMIs, per hypnozoite
389 is in line with other single-cell reports assessing the transcriptomic signatures of non-replicating stages
390 of the parasite's life cycle (Bogale et al., 2021; Howick et al., 2019; Real et al., 2021; Ruberto et al.,
391 2021b), including hypnozoites (Mancio-Silva et al., 2022). Our transcriptome-wide assessment supports
392 the notion that hypnozoites are metabolically active (Adams and Mueller, 2017), demonstrated by the
393 transcription of genes associated with various biological functions including glycolysis and fatty acid
394 metabolism. Furthermore, the expression of genes associated with oxidative stress protection, protein
395 export, mitochondrial respiration, and epigenetic mechanisms such as histone methylation and
396 acetylation, are detectable in hypnozoites, suggesting these parasites are both viable and actively
397 transcribing genes to survive.

398 We also found that hypnozoites exist in various transcriptomic states. We speculate that these
399 differences might represent a spectrum of phenotypes, from persisting to activating. Interestingly, no
400 loss in gene diversity or expression was found in hypnozoites associated with cluster C1 (persisters) in
401 our hypnozoite-directed analysis, suggesting this subpopulation encodes for viable, distinct forms. In
402 the persister hypnozoite cluster, the differential expression of genes encoding for cellular fating RBPs
403 supports the hypothesis that these forms may use post-transcriptional mechanisms to control gene usage
404 (Mueller et al., 2019). The biological significance of the enrichment of genes associated with
405 translational repression, found exclusively in a subpopulation of hypnozoites (C1), suggests this
406 mechanism may govern quiescence, and warrants further investigation.

407 Discerning between non-replicating, uninucleate forms and dead parasites poses a challenge.
408 The absence of a validated hypnozoite viability marker further complicates assessments. These
409 limitations notwithstanding, the data reported here seem to suggest that the transcriptomes assessed
410 represent viable parasites. Similar to a recent study using a non-relapsing rodent malaria model (Afriat
411 et al., 2021), we inferred parasite viability based on visual assessment of fixed cell cultures using an
412 immunofluorescence assay (IFA). For each scRNA-seq library processed, we dedicated cultures from
413 the same infection to provide a visual snapshot of the parasite viability at each end point. While Afriat
414 and colleagues (2021) define abortive forms as displaying "vacuole breakdown," upon inspection of our
415 cultures, we did not find indications of abortive or dead parasites. Moreover, the parasites
416 morphologically identified as hypnozoites were highly similar in morphology to those described in
417 humanized mice (Mikolajczak et al., 2015) and *in vitro* (Roth, Maher et al., 2018). More specifically,
418 they displayed positive *Pv*UIS4 staining for an intact parasitophorous vacuole membrane and a
419 distinctive prominence. These forms have been shown to activate *in vivo* (Mikolajczak et al., 2015) as
420 well as *in vitro* (Maher et al., 2020). Additionally, they have been shown to be susceptible to treatment
421 with primaquine in combination with chloroquine and ionophores, implying they were alive to begin

422 with (Maher et al., 2021). At the molecular level, we did not find consistencies between our data and
423 the transcriptomic signatures of "abortive" *P. berghei* liver forms reported by Afriat and colleagues
424 (2021). For example, orthologous expression of genes encoding for HSP90, HSP70, and HOP—three
425 markers defining abortive parasites in their dataset—displayed greater expression in the schizont cluster
426 relative to hypnozoites. These observations further support the hypothesis that hypnozoite
427 transcriptomes assessesed in this study were derived from viable parasites.

428 We highlight distinct transcriptomic signatures of infected versus non-infected hepatocytes, and
429 show that signaling pathways associated with energy metabolism, antioxidant stress, and immune
430 response are altered in infected hepatocytes. The extent to which individual hepatocytes respond to *P.*
431 *vivax* schizonts and hypnozoites has previously been unknown. A bulk RNA sequencing approach has
432 been used to identify pathways altered in hepatocytes in response to *Plasmodium* infection (LaMonte et
433 al., 2019); however, it is limited insofar as it averages gene expression from millions of cells, obscuring
434 any parasite-specific effects on an infected cell. Targeted approaches have revealed *P. vivax* liver forms
435 recruit host factors to facilitate growth (LaMonte et al., 2019; Posfai et al., 2020), but how certain
436 infected hepatocyte populations contribute to disease transmission, and how hepatocyte subpopulations
437 support development, are intriguing topics for future studies (Vijayan et al., 2021). Our data identify
438 potential host factors essential for *P. vivax*'s successful liver stage development. Whether certain
439 hepatocyte phenotypes influence the development, especially activation of hypnozoites into schizonts,
440 requires further investigation.

441 Several observations suggest protein degradation may be important for the parasite's liver
442 stages. Targeting mechanisms related to this process may therefore be an effective means of killing these
443 forms. For instance, the ability of hepatocytes to uptake and break down hemoglobin (Bissell et al.,
444 1972) supports that this protein substrate could be an essential amino acid source for the parasite. Our
445 data suggest that several mechanisms may allow *P. vivax* to utilize the amino acids derived from this
446 protein; or more broadly, any protein substrate. In hypnozoites, the increased expression of genes
447 encoding for proteases, such as vivapains, supports the idea that these parasites digest host cytosolic
448 proteins**.** The role of these proteins as hemoglobinases have been defined extensively in *P. falciparum*
449 blood stages (Drew et al., 2008; Rosenthal, 2011; Salas et al., 1995). A similar role has been described
450 for *P. vivax* (Byoung-Kuk et al., 2004), but there is limited information about their significance in the
451 liver stages. Interestingly, a recent report using a complementary single-cell capture technology (Hughes
452 et al., 2020) also found that these genes display greater expression in hypnozoites relative to schizonts
453 (Mancio-Silva et al., 2022). Vivapains are highly homologous to cathepsin protease L (TgCpl) in the
454 related apicomplexan *Toxoplasma gondii.* In these parasites, TgCpl is localized to its plant-like vacuolar
455 compartment—a lysosome-like organelle containing a variety of proteases (Parussini et al., 2010)—and
456 one of its functions is to aid in the digestion of host-derived proteins (Dou et al., 2014). Genetic or

457 chemical disruption of TgCpl negatively impacts the viability of bradyzoites, a persisting form of this
458 parasite (di Cristina et al., 2017). Given these orthologous proteins' roles in *P. falciparum* and *T. gondii*,
459 we speculate that the expression of vivapains may support the persistence of *P. vivax* hypnozoites.

460 Persistence of hypnozoites is contingent on the longevity of the hepatocyte in which it resides.
461 The increased expression of genes associated with antioxidant stress (Scarpulla, 2002) is consistent with
462 the hypothesis that hypnozoite infection induces changes in the hepatocyte to promote cell survival, in
463 which NRF2 could be playing a regulatory role (Bindschedler et al., 2022). One host gene upregulated
464 in infected hepatocytes validated by IFA, *AKR1B10*, is regulated by NRF2, which activates protective
465 pathways in response to oxidative stress (Tebay et al., 2015). We also detected genes displaying greater
466 expression in infected hepatocytes regulated by NFYB, a transcription factor important for cell
467 proliferation, mitochondrial integrity, and cellular longevity (Tharyan et al., 2020). At day 5 post-
468 infection, the increased expression of mitochondria-related genes in hepatocytes infected with schizonts
469 may be required to meet the parasite's energy demands during replication, but the enrichment of
470 mitochondria-related genes in cells infected with hypnozoites could also aid in ensuring longevity of the
471 hepatocyte. In addition to these positive regulators of cell survival, we found a decreased expression of
472 genes associated with cell death such as *UBB, UBC,* and *HSP90AB1*, potentially regulated by CEBPD,
473 a transcription factor with a role in cell death (Tsai et al., 2017; Wang et al., 2019).

474 Persistence of hypnozoites also requires evading host detection. Our analyses indicate the
475 parasite alters the host hepatocyte to evade detection by immune cells. First, there is a decrease in
476 expression of genes encoding for chemoattractants (*CCL20, CXCL8, IL32*) in infected hepatocytes, and
477 an increase in expression of PTGR1, a negative regulator of the chemotactic factor leukotriene B4
478 (Yokomizo et al., 1993). These changes would result in decreased secretion of chemokines that recruit
479 innate immune cells to the liver, thereby reducing recruitment of adaptive immune cells like CD8 T-
480 cells that kill infected hepatocytes (Chakravarty et al., 2007). Interestingly, there was also a decrease in
481 expression of MHC-1 molecules (*HLA-A and -B*). The presentation of parasite peptides to be detected
482 by surveying CD8 T-cells would therefore be reduced (Neefjes et al., 2011), creating an additional layer
483 of protection should innate immune cells be recruited, for example upon lysis of the hepatocyte by
484 schizonts. We propose that *P. vivax* infected hepatocytes are re-programmed to prevent recruitment of
485 innate immune cells on the one hand, and to reduce the likelihood of their detection by the adaptive
486 immune system on the other, all to enable progress through schizogony and for hypnozoites to persist
487 undetected. Understanding the mechanisms leading up to this warrant further inversitgation, as their
488 reversal may lead to improved clearance of hypnozoites, thus reducing relapses. Indeed, a vaccine would
489 need to decrease relapses to have an impact on *P. vivax* transmission and disease (White et al., 2017),
490 but the decrease of MHC-I expression in infected hepatocytes may mean that standard focuses to
491 generate CD8 and CD4 polyfunctional T-cells in the liver may not effectively eliminate *P. vivax*. Recent

492 attempts to test anti-relapse vaccine candidates with *P. cynomolgi* did not prevent relapses despite higher
493 inducing IFNγ producing cells, a common metric used as a correlate of protection (Kim et al., 2020),
494 indicating that alternative strategies may be needed.

495 Our transcriptome-wide characterization of schizonts, hypnozoites, and infected hepatocytes
496 highlights transcripts altered during infection, and provides a framework for examining the role of
497 infection dynamics of *P. vivax* liver stages. By examining two early liver stage time points at single-cell
498 resolution, our study lays out a proof of principle and a technical advance demonstrating the importance
499 of *in vitro* models to shed light on the molecular basis of *P. vivax* liver stage development and infection.
500 To conclude, the overall aim of our research was to elucidate the molecular signatures of *P. vivax* liver
501 infection, a better understanding of which will aid in facilitating the development of new therapeutics
502 to ultimately reduce transmission. We anticipate that interventions could involve parasite- and/or host-
503 directed small molecule therapies, both of which our group is actively pursuing. The comprehensive
504 mapping of the transcriptional landscape of both the host and *P. vivax* described here provides an
505 important framework for further investigation.

506 MATERIALS AND METHODS

507 Ethics statement

508 All research procedures were reviewed and approved by the Cambodian National Ethics Committee for
509 Health Research (approval numbers: #113NECHR, #104NECHR and #089NECHR).

510 Blood samples, mosquitos, and infections

511 The complete protocol used for mosquito rearing an infection has been published (Maher et al., 2021).
512 In brief, blood samples from symptomatic patients infected with *P. vivax* were collected at local health
513 facilities in Mondulkiri province in Cambodia from March 2020 to October 2021. Following a *P. vivax*
514 gametocyte-containing blood meal, *An. dirus* mosquitoes were maintained at ambient temperature on a
515 12:12 light: dark cycle and fed 10% sucrose + 0.5% PABA solution. *An. dirus* found positive for *P.*
516 *vivax* oocysts at six-days post-feeding were transported to the Institut Pasteur Cambodia Insectary
517 Facility in Phnom Penh, Cambodia where they were maintained under the same conditions described
518 above.

519 **Sporozoite isolation and primary human hepatocyte infections**

520 The complete protocol used for seeding primary human hepatocytes, harvesting sporozoites, and
521 infecting cultures has been published (Maher et al., 2021). In brief, *P. vivax* sporozoites were isolated
522 from the salivary glands of female *An. dirus* mosquitoes 18 days after an infectious blood-meal. Primary
523 human hepatocytes (Lot BGW, BioIVT) were seeded 2 days before infection with 30,000 sporozoites
524 (replicate 1), or 15,200 sporozoites (replicate 2) per well. Media was replaced with fresh CP media
525 (BioIVT) containing antibiotics (penicillin, streptomycin, and gentamycin) the day after infection and
526 every 2-3 days thereafter. Hepatocytes were treated with 1 µM MMV390048 on days 5, 6, and 7 post-
527 infection to kill replicating schizonts, resulting in cultures with solely hypnozoites at 9 days post-
528 infection. At days 5 and 9 post-infection, cultures were processed for single-cell partitioning (described
529 in the following section) or immunofluorescence assay (IFA). For the latter, hepatocytes were fixed with
530 4% paraformaldehyde in 1X PBS. Fixed cultures were then stained overnight at 4ºC with recombinant
531 mouse anti-*P. vivax* UIS4 antibody (Schäfer et al., 2018) diluted 1:25,000 in a stain buffer (0.03% Triton
532 X-100) and 1% (w/v) BSA in 1X PBS. The following day, cultures were washed three times with 1X
533 PBS and then stained overnight at 4ºC with rabbit anti-mouse AlexaFluor ™488-conjugated antibody
534 (Thermo Fisher) diluted 1:1,000 in stain buffer. Cultures were washed three times with 1X PBS and
535 counterstained with 1 mg/mL Hoechst 33342 (Thermo Fisher) to detect parasite and host DNA. High
536 content imaging was performed on a Lionheart imaging system (Biotek). Quantification of the number
537 of nuclei and parasite liver forms was performed using Gen5 high content analysis software (Biotek).
538 Confocal images were obtained using an ImageXpress Imaging System (Molecular Devices).

539 **Single-cell partitioning, library preparation, and sequencing**

540 Hepatocyte cultures infected with *P. vivax* were processed prior to- and post- MMV390048 treatment
541 (5- and 9-days post-infection, respectively). Two replicate experiments, defined as an independent
542 plating of hepatocytes infected with sporozoites from a unique field isolate, were performed several
543 months apart. Additionally, and as a negative control, one replicate of hepatocyte cultures never exposed
544 to *P. vivax* (naïve) were processed similarly to those that were infected. At each endpoint for each
545 replicate, approximately 640,000 primary human hepatocytes (16 wells of a 384-well plate each having
546 approximately 10,000 cells) were treated with trypsin (Corning 25-053-Cl) to facilitate their detachment
547 from the plate. Once detached, trypsin was inactivated with 1:1 complete media and the cell suspension
548 was collected into a 5mL protein-low bind centrifuge tube (Eppendorf). To remove residual trypsin,
549 hepatocytes were washed via three sequential rounds of pelleting (50 x g, 3 min, 4ºC) and resuspending
550 in 1X PBS containing 0.1% BSA. Cells were then passed through a 35µm strainer (Falcon 352235) to
551 minimize or remove hepatocyte clusters. Prior to partitioning cells on the Chromium controller (10x
552 Genomics), hepatocytes were counted and the cell concentration was assessed using a hemocytometer.

553 Approximately 10,000 hepatocytes were loaded on a Chromium Chip B (10x Genomics) as per
554 manufacturer's recommendations. Chips containing hepatocyte suspensions, Gel Beads in Emulsion
555 (GEMs), and reverse transcription reagents were loaded into the Chromium controller (10x Genomics)
556 for single-cell partitioning and cell barcoding. Barcoded cDNA libraries were generated according to
557 the Chromium Single Cell 3' gene expression protocol (version 3). In total, 6 cDNA libraries were
558 generated (two replicates at 5 days post-infection, two replicates at 9 days post-infection, one uninfected
559 control for day 5 cultures, and one uninfected control for day 9 cultures). Libraries were loaded on
560 individual flow cell lanes and sequenced at a depth of 400 million reads using a HiSeq X Ten platform
561 (Illumina) at Macrogen (Seoul, Korea).

562 **Computational analysis of single-cell RNA sequencing data**

563 Quality control checks on the raw sequencing data were performed using FASTQC (Andrews, 2010).
564 In a manner similar to other host-pathogen single-cell studies (Ren et al., 2021; Szabo et al., 2021), a
565 multi-species transcriptome index containing the transcriptomes for *P. vivax* P01 (PlasmoDB.org,
566 version 51) and *H. sapiens* GRCh8 (Ensembl, version 103) was created using the 'ref' function in kb-
567 python (0.26.3)— a python package that wraps the kallisto | bustools single-cell RNA-seq workflow
568 (Bray et al., 2016; Melsted et al., 2021). The *P. vivax* P01 transcriptome file used for the generation of
569 the multi-species index contained gene regions encoding for UTRs (Siegel, Chappell et al., 2020). Next,
570 using the same package, reads were pseudoaligned and counted using the 'count' function with
571 parameters suitable for sequencing data generated from version 3 of 10x Genomics' 3' gene expression
572 technology: kb count -i human_Pv_index.idx -g t2g.txt -x 10xv3 -t8 -o .
573 /path/to/read/10xV3sequencesread1.fastq.gz path/to/10xV3sequencesread2.fastq.gz. After performing
574 kb count on the sequencing outputs from the 6 single-cell libraries, the resulting unfiltered cell-gene
575 count matrices were read into R (v 4.1.1) for further host and parasite-specific processing described in
576 the following sections.

577 **Filtering and normalization of scRNA-seq count matrices**

578 To distinguish between droplets containing cells and those only with ambient RNA, we used DropUtils'
579 emptyDrops function (Lun et al., 2019) with the lower total UMI count threshold (at or below which all
580 barcodes are assumed to correspond to empty droplets) set to 1,000. The droplets with cells (FDR <
581 0.001), more specifically, those containing barcoded transcripts derived from either human, parasite, or
582 a combination of the two—were kept for downstream processing.

583 **Assessment of *P. vivax* liver stage transcriptomes**

584 For the analyses of *P. vivax*, we filtered out the transcripts derived from human, leaving only transcripts
585 derived from the parasite to be assessed. All samples were processed independently. For each sample,
586 cells with less than 60 genes detected were removed. Next, we filtered out genes with low counts,
587 retaining genes with 10 or greater UMIs across all cells. Post cell and gene filtering, the data were
588 normalized using Seurat (Stuart et al., 2019) 'LogNormalize' function with the default parameters
589 selected.

590 *Data integration and clustering*

591 The data were integrated using Seurat's SCTransform function (Hafemeister and Satija, 2019)
592 with the following parameters indicated: variable.features.n = NULL, variable.features.rv.th = 1.3.
593 Clustering was performed using the Seurat functions FindNeighbours (dims = 1:20) followed by
594 FindClusters (resolution = 0.1, algorithm = 4 for all data or resolution = 0.3, algorithm = 4 for hypnozoite
595 filtered data).

596 *Differential gene expression analysis*

597 To detect differentially expressed genes, the Seurat function FinalAllMarkers and FindMarkers
598 were used. For differential gene expression testing using the FindMarkers function, we used the
599 following parameters: logfc.threshold = 0.0, ident.1 = '1', ident.2 = '2', test.use = "wilcox", min.pct = 0,
600 only.pos = F, assay = "RNA". For differential gene expression testing using the FindAllMarkers
601 function, we used the following parameters: test.use = "wilcox", only.pos = T, assay = "RNA", log2FC
602 = 0.0. For the schizont versus hypnozoite comparisons, genes with a Bonferroni adjusted p value < 0.01
603 & absolute average log2 FC) > 0.5 were used RBP and GO analyses. For the hypnozoite versus
604 hypnozoite comparisions, genes with a Bonferroni adjusted p value of < 0.05 and absolute average log2
605 FC > 0.5 were used for RBP and GO analsysis.

606 *RBP analyses*

607 RBPs with cell fating potential reported in humans (Decker and Parker, n.d.; Gerstberger et al.,
608 2014; Guallar and Wang, 2014; Voronina et al., 2011; Youn et al., 2019) were manually curated. The
609 orthologues of these cell fating RBPs in *P. vivax* were obtained using OrthoMCL (Release-6.8)(Chen
610 et al., 2006). Within the differentially expressed genes, genes encoding for cell fating RBPs were filtered
611 for further assessment.

612 *GO enrichment analyses*

613 GO enrichment analysis was performed on the PlasmoDB (v55) website with the following
614 input parameters selected: P value cutoff = 0.05; Limit to GO Slim terms = No; Evidence: Computed,
615 curated. Enrichment from GO cellular compartment (CC), biological processes (BP), and molecular
616 function (MF) were all assessed. Gene with an Bonferroni adjusted p value < 0.05 were considered
617 significantly enriched.

618 **Assessment of human hepatocyte transcriptomes**

619 For the analyses of hepatocytes, we removed all transcripts derived from *P. vivax*, leaving only the
620 transcripts derived from hepatocytes. We retained transcripts detected in at least 30 cells. Next, cells
621 with less than 1,500 UMIs were removed from further analyses**.** Post-cell and gene filtering, the data
622 from each replicate were normalized using Seurat's 'LogNormalize' function with the default
623 parameters.

624 *Data integration and low dimensional reduction*

625 Filtered, normalized data matrices were integrated in a manner described in in the Seurat
626 (version 4) vignette, *Introduction to scRNA-seq integration*, available on the Sajita Lab's website
627 (https://satijalab.org/seurat/articles/integration_introduction.html). Briefly, integration features were
628 identified in each replicate using the 'SelectIntegrationFeatures' function with the nFeatures parameter
629 set to 3000. Next, we used 'PrepSCTIntegration' to prepare object list containing the 3000 features for
630 integration. We then used 'FindIntegrationAnchors' to identify a set of anchors between datasets with
631 the following parameters specified: normalization.method = "SCT", anchor.features = "features",
632 reference = naïve hepatocytes day 5). Last, using these anchors, the six datasets were integrated using
633 the 'IntegrateData' function with the following parameters specified: normalization.method = "SCT".
634 After integrating the data, we perform dimensionilty reduction using the 'RunPCA' function, followed
635 by 'RunTSNE' with 1:30 dimensions selected.

636 *Gene Ontology and Reactome enrichment analyses*

637 Enriched biological processes and pathways were determined using gProfiler (Raudvere et al.,
638 2019) with the following options selected: ordered query, statistical domain scope—only annotated
639 genes, significance threshold—g:SCS threshold, user threshold—0.05, Gene Ontology—GO biological
640 processes, No electronic GO annotations, biological pathways—Reactome. Transcripts that displayed
641 significant changes in expression in infected hepatocytes versus non-infected hepatocytes were used as
642 input. EnrichmentMap (v 1.1.0) (Merico et al., 2010) for CytoScape (v 3.8.2) (Shannon et al., 2003) was
643 used to create the enrichment networks. Significantly enriched GO biological processes and Reactome
644 pathways (adjusted p value < 0.05) were used as input. Pathways were clustered and annotated using

645 the AutoAnnotate function (Kucera et al., 2016). Node size corresponds to the number of transcripts in
646 the corresponding set, and edge widths correspond to the number of transcripts shared between sets.

647 *Transcription factor enrichment analysis*

648 We downloaded curated sets of known transcription factors from the website
649 (http://amp.pharm.mssm.edu/Enrichr/) (Kuleshov et al., 2016). Transcription factor—target gene sets
650 were obtained by ChIP-X experiments from the ChEA (Lachmann et al., 2010) and ENCODE (Feingold
651 and Pachter, 2004) projects. TF-target relationships using Chip-seq data from ENCODE and CHEA
652 were used to identify overrepresented pathways and TFs. Differentially expressed genes (Bonferroni
653 adjusted p value < 0.05) in each condition versus non-infected cells were used as inputs. Gene sets with
654 an q value < 0.05 were considered significantly enriched.

655 **Carfilzomib dose-response assessment**

656 A carfilzomib dose-response against *P. vivax* liver forms was obtained from three independent
657 experiments, in which a different *P. vivax* clinical isolate was allowed to infect BGW human
658 hepatocytes. The 12-day assay was used (Maher et al., 2021). All independent experiments resulted in
659 sufficient hypnozoite formation within each well for dose-response calculations. Liver stage parasite
660 growth metrics and compound dilutions were loaded into CDD Vault (Collaborative Drug Discovery)
661 and growth data normalized such that zero (negative) inhibition was set as the average of DMSO wells
662 and 100% (positive) inhibition was set to the effective doses of a nigericin control. Normalized values
663 were then combined in Graphpad Prism to fit a dose-response curve and calculated IC_{50} values from all
664 replicates.

665 **Quantification of AKR1B10 protein expression**

666 To analyze AKR1B10 expression and localization, *P. vivax*-infected primary human hepatocytes were
667 fixed 12 days post-infection. Five independent hepatocyte infections were used. Infected wells were
668 then permeabilized for 20 minutes with 0.2% TritonX-100, washed thrice with 1X PBS, and blocked in
669 3% BSA for one hour. Primary antibodies rabbit anti-HsAKR1B10 (PA5-30773, Thermo Fisher) and
670 mouse anti-*Pv*UIS4 were sequentially added, diluted 1:100 and 1:500, respectively. Antibodies were
671 incubated overnight at 4ºC and washed 3 times with 1X PBS before addition of 1:400 Alexa- Fluor 568
672 donkey anti-rabbit for *Hs*AKR1B10 or 1:400 AlexaFluor 488 goat anti-mouse for *Pv*UIS4. Secondary
673 antibodies were incubated overnight at 4ºC. Cells were washed thrice with 1X PBS before adding 0.5
674 mg/mL DAPI for 10 minutes. Cells were washed 3 final times with 1X PBS before image collection

675 with an ImageXpress inverted confocal microscope (Molecular Devices). Image analysis was completed
676 using MetaXpress analysis software (Molecular Devices).

677 **Contact for reagent and resource sharing**

678 Further information and requests for resources and reagents should be directed to and will be fulfilled
679 by the Lead Contact, Dennis Kyle (email: dennis.kyle@uga.edu).

680 **Data availability**

681 All raw sequencing data have been deposited in the European Nucleotide Archive at European
682 Molecular Biology Laboratory European Bioinformatics Institute (www.ebi.ac.uk/ena/) under accession
683 number PRJEB52293. Scripts containing the code used to process the single-cell RNA seq data are
684 available on GitHub at: https://github.com/AnthonyRuberto/Pv_LS_singleCell. Archived scripts (Shell
685 and R) and output files as at time of publication will be made available on Zenodo.

686 **Acknowledgements**

687 We thank the patients of Mondulkiri Province, Cambodia, for participating in this study. We thank the
688 Institut Pasteur du Cambodge's field site manager (Saorin Kim) for logistical assistance, insectary staff
689 (Makara Pring, Koeun Kaing, Nora Sambath) for the *An. dirus* mosquito colony maintenance, and
690 laboratory staff (Eakpor Piv, Chansophea Chhin, Sreyvouch Phen, Chansovandan Chhun, Sivcheng
691 Phal, Baura Tat) for assistance with the mosquito dissections and the *in vitro* assays.

692 High-content imaging data was produced in part by the Biomedical Microscopy Core at the
693 University of Georgia, supported by the Georgia Research Alliance. A.R.J., B.B. and I.M. acknowledge
694 support from the Victorian State Government Operational Infrastructure Support and Australian
695 Government National Health and Medical Research Council Independent Research Institute
696 Infrastructure Support Scheme. This work was also supported by the Agence Nationale de la Recherche
697 (ANR-17-CE13-0025 to A.A.R and I.M.); an Australian National Health and Medical Research Council
698 Leadership Fellowship (APP1194330 to A.R.J.); the Bill & Melinda Gates Foundation (OPP1023601
699 to D.E.K.); and Medicines for Malaria Venture (RD/2017/0042 to B.W. and A.V., RD/16/1082 and
700 RD/15/0022 to S.P.M. and D.E.K.).

701 A.A.R., S.P.M., A.V., I.M., B.W. and D.E.K conceived and designed the study; A.A.R, S.P.M.
702 and A.V. performed the experiments; A.A.R., C.B., B.B. and C.J. curated the data; A.A.R., S.P.M., C.B.,
703 B.B., A.R.J. and C.J. performed the formal analyses; S.P.M., A.V. and I.M., B.W. and D.E.K.

704 coordinated the research activities; S.P.M., A.V., I.M., B.W. and D.E.K. provided resources; S.P.M.
705 and D.E.K. acquired funding for the work; A.A.R wrote the initial draft of the manuscript; all authors
706 reviewed and made contributions to the final version of the manuscript.

707 **REFERENCES**

708 Adams JH, Mueller I. 2017. The Biology of Plasmodium vivax. *Cold Spring Harb Perspect Med*
709 **7**:a025585. doi:10.1101/cshperspect.a025585

710 Adekunle AI, Pinkevych M, McGready R, Luxemburger C, White LJ, Nosten F, Cromer D, Davenport
711 MP. 2015. Modeling the Dynamics of Plasmodium vivax Infection and Hypnozoite Reactivation
712 In Vivo. *PLOS Neglected Tropical Diseases* **9**:e0003595. doi:10.1371/JOURNAL.PNTD.0003595

713 Afriat A, Zuzarte-Luís V, Halpern KB, Buchauer L, Marques S, Lahree A, Amit I, Mota MM, Itzkovitz
714 S. 2021. A spatiotemporally resolved single cell atlas of the Plasmodium liver stage. *bioRxiv*
715 2021.12.03.471111. doi:10.1101/2021.12.03.471111

716 Albuquerque SS, Carret C, Grosso AR, Tarun AS, Peng X, Kappe SHI, Prudêncio M, Mota MM. 2009.
717 Host cell transcriptional profiling during malaria liver stage infection reveals a coordinated and
718 sequential set of biological events. *BMC Genomics* **10**:1–13. doi:10.1186/1471-2164-10-
719 270/FIGURES/6

720 Aldridge S, Teichmann SA. 2020. Single cell transcriptomics comes of age. *Nature Communications*
721 *2020 11:1* **11**:1–4. doi:10.1038/s41467-020-18158-5

722 Balu B, Maher SP, Pance A, Chauhan C, Naumov A v., Andrews RM, Ellis PD, Khan SM, Lin J wen,
723 Janse CJ, Rayner JC, Adams JH. 2011. CCR4-Associated Factor 1 Coordinates the Expression of
724 Plasmodium falciparum Egress and Invasion Proteins. *Eukaryotic Cell* **10**:1257.
725 doi:10.1128/EC.05099-11

726 Battle KE, Karhunen MS, Bhatt S, Gething PW, Howes RE, Golding N, van Boeckel TP, Messina JP,
727 Shanks GD, Smith DL, Baird JK, Hay SI. 2014. Geographical variation in Plasmodium vivax
728 relapse. *Malaria Journal* **13**:1–16. doi:10.1186/1475-2875-13-144/TABLES/5

729 Baumgarten S, Bryant JM, Sinha A, Reyser T, Preiser PR, Dedon PC, Scherf A. 2019. Transcriptome-
730 wide dynamics of extensive m6A mRNA methylation during Plasmodium falciparum blood-stage
731 development. *Nat Microbiol* **4**:2246. doi:10.1038/S41564-019-0521-7

732 Bindschedler A, Schmuckli-Maurer J, Wacker R, Kramer N, Rehmann R, Caldelari R, Heussler VT.
733 2022. Plasmodium berghei-Mediated NRF2 Activation in Infected Hepatocytes Enhances Parasite
734 Survival. *Cellular Microbiology* **2022**:1–17. doi:10.1155/2022/7647976

735 Bissell DM, Hammaker L, Schmid R. 1972. Hemoglobin and Erythrocyte Catabolism in Rat Liver: The
736 Separate Roles of Parenchymal and Sinusoidal Cells. *Blood* **40**:812–822.
737 doi:10.1182/BLOOD.V40.6.812.812

738 Bogale HN, Pascini T v., Kanatani S, Sá JM, Wellems TE, Sinnis P, Vega-Rodríguez J, Serre D. 2021.
739 Transcriptional heterogeneity and tightly regulated changes in gene expression during *Plasmodium*
740 *berghei* sporozoite development. *Proceedings of the National Academy of Sciences*
741 **118**:e2023438118. doi:10.1073/pnas.2023438118

742 Bray NL, Pimentel H, Melsted P, Pachter L. 2016. Near-optimal probabilistic RNA-seq quantification.
743 *Nat Biotechnol* **34**:525–527. doi:10.1038/NBT.3519

744 Bunnik EM, Batugedara G, Saraf A, Prudhomme J, Florens L, le Roch KG. 2016. The mRNA-bound
745 proteome of the human malaria parasite Plasmodium falciparum. *Genome Biol* **17**.
746 doi:10.1186/S13059-016-1014-0

747 Byoung-Kuk NA, Shenai BR, Sijwali PS, Choe Y, Pandey KC, Singh A, Craik CS, Rosenthal PJ. 2004.
748 Identification and biochemical characterization of vivapains, cysteine proteases of the malaria
749 parasite Plasmodium vivax. *Biochemical Journal* **378**:529. doi:10.1042/BJ20031487

750 Caldelari R, Dogga S, Schmid MW, Franke-Fayard B, Janse CJ, Soldati-Favre D, Heussler V. 2019.
751 Transcriptome analysis of Plasmodium berghei during exo-erythrocytic development. *Malaria*
752 *Journal* **18**:330. doi:10.1186/s12936-019-2968-7

753 Chakravarty S, Cockburn IA, Kuk S, Overstreet MG, Sacci JB, Zavala F. 2007. CD8+ T lymphocytes
754 protective against malaria liver stages are primed in skin-draining lymph nodes. *Nature Medicine*
755 *2007 13:9* **13**:1035–1041. doi:10.1038/nm1628

756 Chen F, Mackey AJ, Stoeckert CJ, Roos DS. 2006. OrthoMCL-DB: querying a comprehensive multi-
757 species collection of ortholog groups. *Nucleic Acids Res* **34**. doi:10.1093/NAR/GKJ123

758 Chua ACY, Jie J, Ong Y, Malleret B, Suwanarusk R, Kosaisavee V, Zeeman A-M, Cooper CA, Tan
759 KSW, Zhang R, Tan BH, Abas SN, Yip A, Elliot A, Joyner CJ, Cho JS, Breyer K, Baran S, Lange

760 A, Maher SP, Nosten F, Bodenreider C, Yeung BKS, Mazier D, Galinski MR, Dereuddre-Bosquet
761 N, le Grand R, Kocken CHM, Rénia L, Kyle DE, Diagana TT, Snounou G, Russell B, Bifani P.
762 2019. Robust continuous in vitro culture of the Plasmodium cynomolgi erythrocytic stages. *Nat*
763 *Commun* **10**:1–13. doi:10.1038/s41467-019-11332-4

764 Cogswell FB. 1992. The hypnozoite and relapse in primate malaria. *Clin Microbiol Rev* **5**:26–35.
765 doi:10.1128/CMR.5.1.26

766 Commons RJ, Simpson JA, Watson J, White NJ, Price RN. 2020. Estimating the Proportion of
767 Plasmodium vivax Recurrences Caused by Relapse: A Systematic Review and Meta-Analysis. *Am*
768 *J Trop Med Hyg* **103**:1094–1099. doi:10.4269/AJTMH.20-0186

769 Cubi R, Vembar SS, Biton A, Franetich J-F, Bordessoulles M, Sossau D, Zanghi G, Bosson-Vanga H,
770 Benard M, Moreno A, Dereuddre-Bosquet N, le Grand R, Scherf A, Mazier D. 2017. Laser capture
771 microdissection enables transcriptomic analysis of dividing and quiescent liver stages of
772 Plasmodium relapsing species. *Cellular Microbiology* **19**:e12735. doi:10.1111/cmi.12735

773 Dame JB, Yowell CA, Omara-Opyene L, Carlton JM, Cooper RA, Li T. 2003. Plasmepsin 4, the food
774 vacuole aspartic proteinase found in all Plasmodium spp. infecting man. *Mol Biochem Parasitol*
775 **130**:1–12. doi:10.1016/S0166-6851(03)00137-3

776 Decker CJ, Parker R. n.d. P-Bodies and Stress Granules: Possible Roles in the Control of Translation
777 and mRNA Degradation. doi:10.1101/cshperspect.a012286

778 di Cristina M, Dou Z, Lunghi M, Kannan G, Huynh M-H, McGovern OL, Schultz TL, Schultz AJ,
779 Miller AJ, Hayes BM, van der Linden W, Emiliani C, Bogyo M, Besteiro S, Coppens I, Carruthers
780 VB. 2017. Toxoplasma depends on lysosomal consumption of autophagosomes for persistent
781 infection. doi:10.1038/nmicrobiol.2017.96

782 Díez-Dacal B, Gayarre J, Gharbi S, Timms JF, Coderch C, Gago F, Pérez-Sala D. 2011. Identification
783 of aldo-keto reductase AKR1B10 as a selective target for modification and inhibition by
784 prostaglandin A(1): implications for antitumoral activity. *Cancer Res* **71**:4161–4171.
785 doi:10.1158/0008-5472.CAN-10-3816

786 Dou C, Mcgovern ZL, Cristina D di, Carruthers MB. 2014. Toxoplasma gondii ingests and digests host
787 cytosolic proteins. *mBio* **5**:1188–1202. doi:10.1128/mBio.01188

788 Drew ME, Banerjee R, Uffman EW, Gilbertson S, Rosenthal PJ, Goldberg DE. 2008. Plasmodium Food
789 Vacuole Plasmepsins Are Activated by Falcipains. *The Journal of Biological Chemistry*
790 **283**:12870. doi:10.1074/JBC.M708949200

791 Feingold E, Pachter L. 2004. The ENCODE (ENCyclopedia of DNA Elements) Project. *Science (1979)*
792 **306**:636–640. doi:10.1126/SCIENCE.1105136/SUPPL_FILE/FEINGOLD.SOM.DC2.PDF

793 Foth BJ, Zhang N, Chaal BK, Sze SK, Preiser PR, Bozdech Z. 2011. Quantitative time-course profiling
794 of parasite and host cell proteins in the human malaria parasite Plasmodium falciparum. *Molecular*
795 *and Cellular Proteomics* **10**. doi:10.1074/mcp.M110.006411

796 Fukumoto SI, Yamauchi N, Moriguchi H, Hippo Y, Watanabe A, Shibahara J, Taniguchi H, Ishikawa
797 S, Ito H, Yamamoto S, Iwanari H, Hironaka M, Ishikawa Y, Niki T, Sohara Y, Kodama T,
798 Nishimura M, Fukayama M, Dosaka-Akita H, Aburatani H. 2005. Overexpression of the aldo-keto
799 reductase family protein AKR1B10 is highly correlated with smokers' non-small cell lung
800 carcinomas. *Clin Cancer Res* **11**:1776–1785. doi:10.1158/1078-0432.CCR-04-1238

801 Gerstberger S, Hafner M, Tuschl T. 2014. A census of human RNA-binding proteins. *Nature Reviews*
802 *Genetics 2014 15:12* **15**:829–845. doi:10.1038/nrg3813

803 Govaere O, Cockell S, Tiniakos D, Queen R, Younes R, Vacca M, Alexander L, Ravaioli F, Palmer J,
804 Petta S, Boursier J, Rosso C, Johnson K, Wonders K, Day CP, Ekstedt M, Orešič M, Darlay R,
805 Cordell HJ, Marra F, Vidal-Puig A, Bedossa P, Schattenberg JM, Clément K, Allison M, Bugianesi
806 E, Ratziu V, Daly AK, Anstee QM. 2020. Transcriptomic profiling across the nonalcoholic fatty
807 liver disease spectrum reveals gene signatures for steatohepatitis and fibrosis. *Sci Transl Med* **12**.
808 doi:10.1126/SCITRANSLMED.ABA4448

809 Guallar D, Wang J. 2014. RNA-binding proteins in pluripotency, differentiation, and reprogramming.
810 *Frontiers in Biology* **9**:389–409. doi:10.1007/s11515-014-1326-y

811 Gupta DK, Dembele L, Voorberg-Van Der Wel A, Roma G, Yip A, Chuenchob V, Kangwanrangsan N,
812 Ishino T, Vaughan AM, Kappe SH, Flannery EL, Sattabongko J, Mikolajczak S, Bifani P, Kocken
813 CHM, Diagana TT. 2019. The plasmodium liver-specific protein 2 (LISP2) is an early marker of
814 liver stage development. *Elife* **8**. doi:10.7554/ELIFE.43362

815 Gural N, Mancio-Silva L, Miller AB, Galstian A, Butty VL, Levine SS, Patrapuvich R, Desai SP,
816 Mikolajczak SA, Kappe SHI, Fleming HE, March S, Sattabongkot J, Bhatia SN. 2018. In Vitro

817 Culture, Drug Sensitivity, and Transcriptome of Plasmodium Vivax Hypnozoites. *Cell Host*
818 *Microbe* **23**:395-406.e4. doi:10.1016/j.chom.2018.01.002

819 Hafemeister C, Satija R. 2019. Normalization and variance stabilization of single-cell RNA-seq data
820 using regularized negative binomial regression. *Genome Biology* **20**:1–15. doi:10.1186/S13059-
821 019-1874-1/FIGURES/6

822 Hayes JD, Dinkova-Kostova AT. 2014. The Nrf2 regulatory network provides an interface between
823 redox and intermediary metabolism. *Trends in Biochemical Sciences* **39**:199–218.
824 doi:10.1016/J.TIBS.2014.02.002

825 Hentze MW, Castello A, Schwarzl T, Preiss T. 2018. A brave new world of RNA-binding proteins.
826 *Nature Reviews Molecular Cell Biology 2018 19:5* **19**:327–341. doi:10.1038/nrm.2017.130

827 Hollingdale MR, Collins WE, Campbell C, Schwartz AL. 1985. In vitro culture of two populations
828 (dividing and nondividing) of exoerythrocytic parasites of Plasmodium vivax. *Am J Trop Med Hyg*
829 **34**:216–222. doi:10.4269/AJTMH.1985.34.216

830 Howick VM, Russell AJC, Andrews T, Heaton H, Reid AJ, Natarajan K, Butungi H, Metcalf T, Verzier
831 LH, Rayner JC, Berriman M, Herren JK, Billker O, Hemberg M, Talman AM, Lawniczak MKN.
832 2019. The Malaria Cell Atlas: Single parasite transcriptomes across the complete Plasmodium life
833 cycle. *Science* **365**:eaaw2619. doi:10.1126/science.aaw2619

834 Hughes TK, Wadsworth MH, Gierahn TM, Do T, Weiss D, Andrade PR, Ma F, de Andrade Silva BJ,
835 Shao S, Tsoi LC, Ordovas-Montanes J, Gudjonsson JE, Modlin RL, Love JC, Shalek AK. 2020.
836 Second-Strand Synthesis-Based Massively Parallel scRNA-Seq Reveals Cellular States and
837 Molecular Features of Human Inflammatory Skin Pathologies. *Immunity* **53**:878-894.e7.
838 doi:10.1016/J.IMMUNI.2020.09.015

839 Huldén Lena, Huldén Larry, Heliövaara K. 2008. Natural relapses in vivax malaria induced by
840 Anopheles mosquitoes. *Malaria Journal* **7**:1–11. doi:10.1186/1475-2875-7-64/FIGURES/10

841 Itoe MA, Sampaio JL, Cabal GG, Real E, Zuzarte-Luis V, March S, Bhatia SN, Frischknecht F, Thiele
842 C, Shevchenko A, Mota MM. 2014. Host Cell Phosphatidylcholine Is a Key Mediator of Malaria
843 Parasite Survival during Liver Stage Infection. *Cell Host & Microbe* **16**:778.
844 doi:10.1016/J.CHOM.2014.11.006

845 Jin J, Krishack P, Cao D. 2006. Role of aldo-keto reductases in development of prostate and breast
846 cancer. *Front Biosci* **11**:2767–2773. doi:10.2741/2006

847 Kim YC, Dema B, Rodriguez-Garcia R, López-Camacho C, Leoratti FMS, Lall A, Remarque EJ,
848 Kocken CHM, Reyes-Sandoval A. 2020. Evaluation of Chimpanzee Adenovirus and MVA
849 Expressing TRAP and CSP from Plasmodium cynomolgi to Prevent Malaria Relapse in Nonhuman
850 Primates. *Vaccines (Basel)* **8**:1–14. doi:10.3390/VACCINES8030363

851 Kivioja T, Vähärautio A, Karlsson K, Bonke M, Enge M, Linnarsson S, Taipale J. 2011. Counting
852 absolute numbers of molecules using unique molecular identifiers. *Nature Methods* **9**:72–74.
853 doi:10.1038/nmeth.1778

854 Klein AM, Mazutis L, Akartuna I, Tallapragada N, Veres A, Li V, Peshkin L, Weitz DA, Kirschner
855 MW. 2015. Droplet barcoding for single-cell transcriptomics applied to embryonic stem cells. *Cell*
856 **161**:1187–1201. doi:10.1016/j.cell.2015.04.044

857 Kortuem KM, Stewart AK. 2013. Carfilzomib. *Blood* **121**:893–897. doi:10.1182/BLOOD-2012-10-
858 459883

859 Krotoski WA, Collins WE, Bray RS, Garnham PC, Cogswell FB, Gwadz RW, Killick-Kendrick R, Wolf
860 R, Sinden R, Koontz LC, Stanfill PS. 1982. Demonstration of hypnozoites in sporozoite-
861 transmitted Plasmodium vivax infection. *Am J Trop Med Hyg* **31**:1291–1293.
862 doi:10.4269/AJTMH.1982.31.1291

863 Krotoski WA, Garnham PCC, Cogswell FB, Collins WE, Bray RS, Gwasz RW, Killick-Kendrick R,
864 Wolf RH, Sinden R, Hollingdale M. 1986. Observations on early and late post-sporozoite tissue
865 stages in primate malaria. IV. Pre-erythrocytic schizonts and/or hypnozoites of Chesson and North
866 Korean strains of Plasmodium vivax in the chimpanzee. *American Journal of Tropical Medicine*
867 *and Hygiene* **35**:263–274. doi:10.4269/AJTMH.1986.35.263

868 Kucera M, Isserlin R, Arkhangorodsky A, Bader GD. 2016. AutoAnnotate: A Cytoscape app for
869 summarizing networks with semantic annotations. *F1000Res* **5**.
870 doi:10.12688/F1000RESEARCH.9090.1

871 Kuleshov M v., Jones MR, Rouillard AD, Fernandez NF, Duan Q, Wang Z, Koplev S, Jenkins SL,
872 Jagodnik KM, Lachmann A, McDermott MG, Monteiro CD, Gundersen GW, Ma'ayan A. 2016.

Enrichr: a comprehensive gene set enrichment analysis web server 2016 update. *Nucleic Acids Res* **44**:W90–W97. doi:10.1093/NAR/GKW377

Lachmann A, Xu H, Krishnan J, Berger SI, Mazloom AR, Ma'ayan A. 2010. ChEA: transcription factor regulation inferred from integrating genome-wide ChIP-X experiments. *Bioinformatics* **26**:2438–2444. doi:10.1093/BIOINFORMATICS/BTQ466

LaMonte GM, Orjuela-Sanchez P, Calla J, Wang LT, Li S, Swann J, Cowell AN, Zou BY, Abdel-Haleem Mohamed AM, Villa Galarce ZH, Moreno M, Tong Rios C, Vinetz JM, Lewis N, Winzeler EA. 2019. Dual RNA-seq identifies human mucosal immunity protein Mucin-13 as a hallmark of Plasmodium exoerythrocytic infection. *Nature Communications* **10**:488. doi:10.1038/s41467-019-08349-0

le Roch KG, Johnson JR, Florens L, Zhou Y, Santrosyan A, Grainger M, Yan SF, Williamson KC, Holder AA, Carucci DJ, Yates JR, Winzeler EA. 2004. Global analysis of transcript and protein levels across the Plasmodium falciparum life cycle. *Genome Research* **14**:2308–2318. doi:10.1101/GR.2523904

Liehl P, Mota MM. 2012. Innate recognition of malarial parasites by mammalian hosts. *International Journal for Parasitology* **42**:557–566. doi:10.1016/J.IJPARA.2012.04.006

Liehl P, Zuzarte-Luís V, Chan J, Zillinger T, Baptista F, Carapau D, Konert M, Hanson KK, Carret C, Lassnig C, Müller M, Kalinke U, Saeed M, Chora AF, Golenbock DT, Strobl B, Prudêncio M, Coelho LP, Kappe SH, Superti-Furga G, Pichlmair A, Vigário AM, Rice CM, Fitzgerald KA, Barchet W, Mota MM. 2013. Host-cell sensors for Plasmodium activate innate immunity against liver-stage infection. *Nature Medicine 2013 20:1* **20**:47–53. doi:10.1038/nm.3424

Lun ATL, Riesenfeld S, Andrews T, Dao TP, Gomes T, Marioni JC. 2019. EmptyDrops: distinguishing cells from empty droplets in droplet-based single-cell RNA sequencing data. *Genome Biology* **20**:63. doi:10.1186/s13059-019-1662-y

Lysenko Ja. A, Beljaev AE, Rybalka VM. 1977. Population studies of Plasmodium vivax: 1. The theory of polymorphism of sporozoites and epidemiological phenomena of tertian malaria. *Bull World Health Organ* **55**:541.

Macosko EZ, Basu A, Satija R, Nemesh J, Shekhar K, Goldman M, Tirosh I, Bialas AR, Kamitaki N, Martersteck EM, Trombetta JJ, Weitz DA, Sanes JR, Shalek AK, Regev A, McCarroll SA. 2015.

902 Highly Parallel Genome-wide Expression Profiling of Individual Cells Using Nanoliter Droplets.
903 *Cell* **161**:1202–1214. doi:10.1016/J.CELL.2015.05.002

904 MacParland SA, Liu JC, Ma X-Z, Innes BT, Bartczak AM, Gage BK, Manuel J, Khuu N, Echeverri J,
905 Linares I, Gupta R, Cheng ML, Liu LY, Camat D, Chung SW, Seliga RK, Shao Z, Lee E, Ogawa
906 S, Ogawa M, Wilson MD, Fish JE, Selzner M, Ghanekar A, Grant D, Greig P, Sapisochin G,
907 Selzner N, Winegarden N, Adeyi O, Keller G, Bader GD, McGilvray ID. 2018. Single cell RNA
908 sequencing of human liver reveals distinct intrahepatic macrophage populations. *Nature*
909 *Communications* **9**:4383. doi:10.1038/s41467-018-06318-7

910 Maher S, Vantaux A, Cooper C, Chasen N, Cheng W, Joyner C, Manetsch R, Witkowski B, Kyle D.
911 2021. A Phenotypic Screen for the Liver Stages of Plasmodium vivax. *BIO-PROTOCOL* **11**.
912 doi:10.21769/BIOPROTOC.4253

913 Maher SP, Conway AJ, Roth A, Adapa SR, Cualing P, Andolina C, Hsiao J, Turgeon J, Chaumeau V,
914 Johnson M, Palmiotti C, Singh N, Barnes SJ, Patel R, van Grod V, Carter R, Sun H-CS,
915 Sattabongkot J, Campo B, Nosten F, Saadi WM, Adams JH, Jiang RHY, Kyle DE. 2020. An
916 adaptable soft-mold embossing process for fabricating optically-accessible, microfeature-based
917 culture systems and application toward liver stage antimalarial compound testing. *Lab on a Chip*.
918 doi:10.1039/C9LC00921C

919 Maher SP, Vantaux A, Chaumeau V, Chua ACY, Cooper CA, Andolina C, Péneau J, Rouillier M,
920 Rizopoulos Z, Phal S, Piv E, Vong C, Phen S, Chhin C, Tat B, Ouk S, Doeurk B, Kim S, Suriyakan
921 S, Kittiphanakun P, Awuku NA, Conway AJ, Jiang RHY, Russell B, Bifani P, Campo B, Nosten
922 F, Witkowski B, Kyle DE. 2021. Probing the distinct chemosensitivity of Plasmodium vivax liver
923 stage parasites and demonstration of 8-aminoquinoline radical cure activity in vitro. *Sci Rep* **11**.
924 doi:10.1038/S41598-021-99152-9

925 Mancio-Silva L, Gural N, Real E, Wadsworth MH, Butty VL, March S, Nerurkar N, Hughes TK,
926 Roobsoong W, Fleming HE, Whittaker CA, Levine SS, Sattabongkot J, Shalek AK, Bhatia SN.
927 2022. A single-cell liver atlas of Plasmodium vivax infection. *Cell Host & Microbe*.
928 doi:10.1016/J.CHOM.2022.03.034

929 Martin HJ, Maser E. 2009. Role of human aldo–keto-reductase AKR1B10 in the protection against toxic
930 aldehydes. *Chemico-Biological Interactions* **178**:145–150. doi:10.1016/J.CBI.2008.10.021

931 Melsted P, Booeshaghi AS, Liu L, Gao F, Lu L, Min KH (Joseph), da Veiga Beltrame E, Hjörleifsson
932 KE, Gehring J, Pachter L. 2021. Modular, efficient and constant-memory single-cell RNA-seq
933 preprocessing. *Nature Biotechnology 2021 39:7* **39**:813–818. doi:10.1038/s41587-021-00870-2

934 Merico D, Isserlin R, Stueker O, Emili A, Bader GD. 2010. Enrichment Map: A Network-Based Method
935 for Gene-Set Enrichment Visualization and Interpretation. *PLOS ONE* **5**:e13984.
936 doi:10.1371/JOURNAL.PONE.0013984

937 Miao J, Li J, Fan Q, Li Xiaolian, Li Xinyi, Cui L. 2010. The Puf-family RNA-binding protein PfPuf2
938 regulates sexual development and sex differentiation in the malaria parasite Plasmodium
939 falciparum. *Journal of Cell Science* **123**:1039. doi:10.1242/JCS.059824

940 Mikolajczak SA, Vaughan AM, Kangwanrangsan N, Roobsoong W, Fishbaugher M, Yimamnuaychok
941 N, Rezakhani N, Lakshmanan V, Singh N, Kaushansky A, Camargo N, Baldwin M, Lindner SE,
942 Adams JH, Sattabongkot J, Kappe SHI. 2015. Plasmodium vivax liver stage development and
943 hypnozoite persistence in human liver-chimeric mice. *Cell Host Microbe* **17**:526–535.
944 doi:10.1016/J.CHOM.2015.02.011

945 Miller JL, Sack BK, Baldwin M, Vaughan AM, Kappe SHI. 2014. Interferon-Mediated Innate Immune
946 Responses against Malaria Parasite Liver Stages. *Cell Reports* **7**:436–447.
947 doi:10.1016/J.CELREP.2014.03.018

948 Mueller I, Jex AR, Kappe SHI, Mikolajczak SA, Sattabongkot J, Patrapuvich R, Lindner S, Flannery
949 EL, Koepfli C, Ansell B, Lerch A, Emery-Corbin SJ, Charnaud S, Smith J, Merrienne N,
950 Swearingen KE, Moritz RL, Petter M, Duffy MF, Chuenchob V. 2019. Transcriptome and histone
951 epigenome of Plasmodium vivax salivary-gland sporozoites point to tight regulatory control and
952 mechanisms for liver-stage differentiation in relapsing malaria. *International Journal for*
953 *Parasitology* **49**:501–513. doi:10.1016/J.IJPARA.2019.02.007

954 Neefjes J, Jongsma MLM, Paul P, Bakke O. 2011. Towards a systems understanding of MHC class I
955 and MHC class II antigen presentation. *Nature Reviews Immunology 2011 11:12* **11**:823–836.
956 doi:10.1038/nri3084

957 Paquet T, le Manach C, Cabrera DG, Younis Y, Henrich PP, Abraham TS, Lee MCS, Basak R, Ghidelli-
958 Disse S, Lafuente-Monasterio MJ, Bantscheff M, Ruecker A, Blagborough AM, Zakutansky SE,
959 Zeeman AM, White KL, Shackleford DM, Mannila J, Morizzi J, Scheurer C, Angulo-Barturen I,
960 Santosmartínez M, Ferrer S, Sanz LM, Gamo FJ, Reader J, Botha M, Dechering KJ, Sauerwein

961 RW, Tungtaeng A, Vanachayangkul P, Lim CS, Burrows J, Witty MJ, Marsh KC, Bodenreider C,
962 Rochford R, Solapure SM, Jiménez-Díaz MB, Wittlin S, Charman SA, Donini C, Campo B,
963 Birkholtz LM, Khanson K, Drewes G, Kocken CM, Delves MJ, Leroy D, Fidock DA, Waterson
964 D, Street LJ, Chibale K. 2017. Antimalarial efficacy of MMV390048, an inhibitor of Plasmodium
965 phosphatidylinositol 4-kinase. *Science Translational Medicine* **9**.
966 doi:10.1126/SCITRANSLMED.AAD9735/SUPPL_FILE/AAD9735_TABLES_S26_AND_S27.
967 ZIP

968 Parussini F, Coppens I, Shah PP, Diamond SL, Carruthers VB. 2010. Cathepsin L Occupies a Vacuolar
969 Compartment and is a Protein Maturase within the Endo/Exocytic System of Toxoplasma gondii.
970 *Mol Microbiol* **76**:1340. doi:10.1111/J.1365-2958.2010.07181.X

971 Penaranda C, Hung DT. 2019. Single-Cell RNA Sequencing to Understand Host–Pathogen Interactions.
972 *ACS Infectious Diseases* **5**:336–344. doi:10.1021/ACSINFECDIS.8B00369

973 Poran A, Nötzel C, Aly O, Mencia-Trinchant N, Harris CT, Guzman ML, Hassane DC, Elemento O,
974 Kafsack BFC. 2017. Single-cell RNA sequencing reveals a signature of sexual commitment in
975 malaria parasites. *Nature* **551**:95–99. doi:10.1038/nature24280

976 Posfai D, Maher SP, Roesch C, Vantaux A, Sylvester K, Péneau J, Popovici J, Kyle DE, Witkowski B,
977 Derbyshire ER. 2020. Plasmodium vivax Liver and Blood Stages Recruit the Druggable Host
978 Membrane Channel Aquaporin-3. *Cell Chemical Biology*. doi:10.1016/j.chembiol.2020.03.009

979 Qu J, Li J, Zhang Y, He R, Liu X, Gong K, Duan L, Luo W, Hu Z, Wang G, Xia C, Luo D. 2021.
980 AKR1B10 promotes breast cancer cell proliferation and migration via the PI3K/AKT/NF-κB
981 signaling pathway. *Cell & Bioscience* **11**:163. doi:10.1186/S13578-021-00677-3

982 Raudvere U, Kolberg L, Kuzmin I, Arak T, Adler P, Peterson H, Vilo J. 2019. g:Profiler: a web server
983 for functional enrichment analysis and conversions of gene lists (2019 update). *Nucleic Acids*
984 *Research* **47**:W191–W198. doi:10.1093/NAR/GKZ369

985 Real E, Howick VM, Dahalan FA, Witmer K, Cudini J, Andradi-Brown C, Blight J, Davidson MS,
986 Dogga SK, Reid AJ, Baum J, Lawniczak MKN. 2021. A single-cell atlas of Plasmodium
987 falciparum transmission through the mosquito. *Nature Communications 2021 12:1* **12**:1–13.
988 doi:10.1038/s41467-021-23434-z

989 Reid AJ, Talman AM, Bennett HM, Gomes AR, Sanders MJ, Illingworth CJR, Billker O, Berriman M,
990 Lawniczak MKN. 2018. Single-cell RNA-seq reveals hidden transcriptional variation in malaria
991 parasites. *Elife* **7**:1–29. doi:10.7554/eLife.33105

992 Ren X, Wen W, Fan X, Hou W, Su Bin, Cai P, Li J, Liu Y, Tang F, Zhang F, Yang Y, He Jiangping,
993 Ma W, He Jingjing, Wang P, Cao Q, Chen F, Chen Y, Cheng X, Deng G, Deng X, Ding W, Feng
994 Y, Gan R, Guo C, Guo W, He S, Jiang C, Liang J, Li Y min, Lin J, Ling Y, Liu H, Liu J, Liu N,
995 Liu SQ, Luo M, Ma Q, Song Q, Sun W, Wang GX, Wang F, Wang Y, Wen X, Wu Q, Xu G, Xie
996 X, Xiong X, Xing X, Xu H, Yin C, Yu D, Yu K, Yuan J, Zhang B, Zhang P, Zhang T, Zhao J,
997 Zhao Peidong, Zhou J, Zhou W, Zhong S, Zhong X, Zhang S, Zhu L, Zhu P, Zou B, Zou J, Zuo Z,
998 Bai F, Huang X, Zhou P, Jiang Q, Huang Z, Bei JX, Wei L, Bian XW, Liu X, Cheng T, Li X, Zhao
999 Pingsen, Wang FS, Wang H, Su Bing, Zhang Zheng, Qu K, Wang X, Chen J, Jin R, Zhang Zemin.
1000 2021. COVID-19 immune features revealed by a large-scale single-cell transcriptome atlas. *Cell*
1001 **184**:1895-1913.e19. doi:10.1016/J.CELL.2021.01.053

1002 Robinson LJ, Wampfler R, Betuela I, Karl S, White MT, Li Wai Suen CSN, Hofmann NE, Kinboro B,
1003 Waltmann A, Brewster J, Lorry L, Tarongka N, Samol L, Silkey M, Bassat Q, Siba PM, Schofield
1004 L, Felger I, Mueller I. 2015. Strategies for understanding and reducing the Plasmodium vivax and
1005 Plasmodium ovale hypnozoite reservoir in Papua New Guinean children: a randomised placebo-
1006 controlled trial and mathematical model. *PLoS Med* **12**. doi:10.1371/JOURNAL.PMED.1001891

1007 Rosenthal PJ. 2011. Falcipains and Other Cysteine Proteases of Malaria Parasites. *Advances in*
1008 *Experimental Medicine and Biology* **712**:30–48. doi:10.1007/978-1-4419-8414-2_3

1009 Roth A, Maher SP, Conway AJ, Ubalee R, Chaumeau V, Andolina C, Kaba SA, Vantaux A, Bakowski
1010 MA, Thomson-Luque R, Adapa SR, Singh N, Barnes SJ, Cooper CA, Rouillier M, McNamara
1011 CW, Mikolajczak SA, Sather N, Witkowski B, Campo B, Kappe SHI, Lanar DE, Nosten F,
1012 Davidson S, Jiang RHY, Kyle DE, Adams JH. 2018. A comprehensive model for assessment of
1013 liver stage therapies targeting Plasmodium vivax and Plasmodium falciparum. *Nature*
1014 *Communications* **9**:1837. doi:10.1038/s41467-018-04221-9

1015 Ruberto AA, Bourke C, Merienne N, Obadia T, Amino R, Mueller I. 2021a. Single-cell RNA
1016 sequencing reveals developmental heterogeneity among Plasmodium berghei sporozoites.
1017 *Scientific Reports* **11**:4127. doi:10.1038/s41598-021-82914-w

1018 Ruberto AA, Bourke C, Vantaux A, Maher SP, Jex A, Witkowski B, Snounou G, Mueller I. 2021b.
1019 Single-cell RNA sequencing of Plasmodium vivax sporozoites reveals stage- and species-specific
1020 transcriptomic signatures. *bioRxiv* 2021.11.24.469176. doi:10.1101/2021.11.24.469176

1021 Sà JM, Cannon M v., Caleon RL, Wellems TE, Serre D. 2020. Single-cell transcription analysis of
1022 Plasmodium vivax blood-stage parasites identifies stage- and species-specific profiles of
1023 expression. *PLOS Biology* **18**:e3000711. doi:10.1371/journal.pbio.3000711

1024 Salas F, Fichmann J, Lee GK, Scott MD, Rosenthal PJ. 1995. Functional expression of falcipain, a
1025 Plasmodium falciparum cysteine proteinase, supports its role as a malarial hemoglobinase.
1026 *Infection and Immunity* **63**:2120. doi:10.1128/iai.63.6.2120-2125.1995

1027 Sattabongkot J, Yimamnuaychoke N, Leelaudomlipi S, Rasameesoraj M, Jenwithisuk R, Coleman RE,
1028 Udomsangpetch R, Cui L, Brewer TG. 2006. Establishment of a human hepatocyte line that
1029 supports in vitro development of the exo-erythrocytic stages of the malaria parasites Plasmodium
1030 falciparum and P. vivax. *Am J Trop Med Hyg* **74**:708–715.

1031 Scarpulla RC. 2002. Transcriptional activators and coactivators in the nuclear control of mitochondrial
1032 function in mammalian cells. *Gene* **286**:81–89. doi:10.1016/S0378-1119(01)00809-5

1033 Schäfer C, Dambrauskas N, Steel RW, Carbonetti S, Chuenchob V, Flannery EL, Vigdorovich V, Oliver
1034 BG, Roobsoong W, Maher SP, Kyle D, Sattabongkot J, Kappe SHI, Mikolajczak SA, Sather DN.
1035 2018. A recombinant antibody against Plasmodium vivax UIS4 for distinguishing replicating from
1036 dormant liver stages. *Malaria Journal* **17**:370. doi:10.1186/S12936-018-2519-7

1037 Schäfer C, Roobsoong W, Sattabongkot J, Mikolajczak SA, Kappe SHI. 2020. A Humanized Mouse
1038 Model for Plasmodium vivax to Test Interventions that Block Liver Stage to Blood Stage
1039 Transition and Blood Stage Infection. *iScience* **23**:101381. doi:10.1016/j.isci.2020.101381

1040 Schäfer C, Zanghi G, Vaughan AM, Kappe SHI. 2021. Plasmodium vivax Latent Liver Stage Infection
1041 and Relapse: Biological Insights and New Experimental Tools. doi:10.1146/annurev-micro-
1042 032421

1043 Shannon P, Markiel A, Ozier O, Baliga NS, Wang JT, Ramage D, Amin N, Schwikowski B, Ideker T.
1044 2003. Cytoscape: A Software Environment for Integrated Models of Biomolecular Interaction
1045 Networks. *Genome Res* **13**:2498–2504. doi:10.1101/gr.1239303

1046 Siegel S v., Chappell L, Hostetler JB, Amaratunga C, Suon S, Böhme U, Berriman M, Fairhurst RM,
1047 Rayner JC. 2020. Analysis of Plasmodium vivax schizont transcriptomes from field isolates
1048 reveals heterogeneity of expression of genes involved in host-parasite interactions. *Scientific*
1049 *Reports* **10**:16667. doi:10.1038/s41598-020-73562-7

1050 Singh AP, Buscaglia CA, Wang Q, Levay A, Nussenzweig DR, Walker JR, Winzeler EA, Fujii H,
1051 Fontoura BMA, Nussenzweig V. 2007. Plasmodium Circumsporozoite Protein Promotes the
1052 Development of the Liver Stages of the Parasite. *Cell* **131**:492–504.
1053 doi:10.1016/J.CELL.2007.09.013

1054 Stuart T, Butler A, Hoffman P, Hafemeister C, Papalexi E, Mauck WM, Hao Y, Stoeckius M, Smibert
1055 P, Satija R. 2019. Comprehensive Integration of Single-Cell Data. *Cell* **177**:1888-1902.e21.
1056 doi:10.1016/j.cell.2019.05.031

1057 Szabo PA, Dogra P, Gray JI, Wells SB, Connors TJ, Weisberg SP, Krupska I, Matsumoto R, Poon
1058 MML, Idzikowski E, Morris SE, Pasin C, Yates AJ, Ku A, Chait M, Davis-Porada J, Guo X v.,
1059 Zhou J, Steinle M, Mackay S, Saqi A, Baldwin MR, Sims PA, Farber DL. 2021. Longitudinal
1060 profiling of respiratory and systemic immune responses reveals myeloid cell-driven lung
1061 inflammation in severe COVID-19. *Immunity* **54**:797-814.e6.
1062 doi:10.1016/J.IMMUNI.2021.03.005

1063 Tarun AS, Peng X, Dumpit RF, Ogata Y, Silva-Rivera H, Camargo N, Daly TM, Bergman LW, Kappe
1064 SHI. 2008. A combined transcriptome and proteome survey of malaria parasite liver stages.
1065 *Proceedings of the National Academy of Sciences* **105**:305–310. doi:10.1073/PNAS.0710780104

1066 Tebay LE, Robertson H, Durant ST, Vitale SR, Penning TM, Dinkova-Kostova AT, Hayes JD. 2015.
1067 Mechanisms of activation of the transcription factor Nrf2 by redox stressors, nutrient cues, and
1068 energy status and the pathways through which it attenuates degenerative disease. *Free Radic Biol*
1069 *Med* **88**:108. doi:10.1016/J.FREERADBIOMED.2015.06.021

1070 Tharyan RG, Annibal A, Schiffer I, Laboy R, Atanassov I, Weber AL, Gerisch B, Antebi A. 2020.
1071 NFYB-1 regulates mitochondrial function and longevity via lysosomal prosaposin. *Nature*
1072 *Metabolism* **2**:387–396. doi:10.1038/s42255-020-0200-2

1073 Toro-Moreno M, Sylvester K, Srivastava T, Posfai D, Derbyshire ER. 2020. RNA-Seq Analysis
1074 Illuminates the Early Stages of Plasmodium Liver Infection. doi:10.1128/mBio.03234-19

1075 Traag VA, Waltman L, van Eck NJ. 2019. From Louvain to Leiden: guaranteeing well-connected
1076 communities. *Scientific Reports* **9**:1–12. doi:10.1038/s41598-019-41695-z

1077 Tsai HH, Lai HY, Chen YC, Li CF, Huang HS, Liu HS, Tsai YS, Wang JM. 2017. Metformin promotes
1078 apoptosis in hepatocellular carcinoma through the CEBPD-induced autophagy pathway.
1079 *Oncotarget* **8**:13832. doi:10.18632/ONCOTARGET.14640

1080 Tucker M, Valencia-Sanchez MA, Staples RR, Chen J, Denis CL, Parker R. 2001. The transcription
1081 factor associated Ccr4 and Caf1 proteins are components of the major cytoplasmic mRNA
1082 deadenylase in Saccharomyces cerevisiae. *Cell* **104**:377–386. doi:10.1016/S0092-8674(01)00225-
1083 2

1084 Ungureanu E, Killick-Kendrick R, Garnham PCC, Branzei P, Romanescu C, Shute PG. 1976. Prepatent
1085 periods of a tropical strain of Plasmodium vivax after inoculations of tenfold dilutions of
1086 sporozoites. *Trans R Soc Trop Med Hyg* **70**:482–483. doi:10.1016/0035-9203(76)90133-4

1087 Vembar SS, Droll D, Scherf A. 2016. Translational regulation in blood stages of the malaria parasite
1088 Plasmodium spp.: systems-wide studies pave the way. *Wiley Interdisciplinary Reviews RNA* **7**:772.
1089 doi:10.1002/WRNA.1365

1090 Vijayan K, Wei L, Glennon EKK, Mattocks C, Bourgeois N, Staker B, Kaushansky A. 2021. Host-
1091 targeted Interventions as an Exciting Opportunity to Combat Malaria. *Chemical Reviews*
1092 **121**:10452–10468. doi:10.1021/acs.chemrev.1c00062

1093 Voorberg-van der Wel A, Roma G, Gupta DK, Schuierer S, Nigsch F, Carbone W, Zeeman AM, Lee
1094 BH, Hofman SO, Faber BW, Knehr J, Pasini E, Kinzel B, Bifani P, Bonamy GMC, Bouwmeester
1095 T, Kocken CHM, Diagana TT. 2017. A comparative transcriptomic analysis of replicating and
1096 dormant liver stages of the relapsing malaria parasite plasmodium cynomolgi. *Elife* **6**.
1097 doi:10.7554/eLife.29605.001

1098 Voorberg-van der Wel AM, Zeeman AM, Nieuwenhuis IG, van der Werff NM, Klooster EJ, Klop O,
1099 Vermaat LC, Kumar Gupta D, Dembele L, Diagana TT, Kocken CHM. 2020. A dual fluorescent
1100 Plasmodium cynomolgi reporter line reveals in vitro malaria hypnozoite reactivation.
1101 *Communications Biology* **3**. doi:10.1038/s42003-019-0737-3

1102 Voronina E, Seydoux G, Sassone-Corsi P, Nagamori I. 2011. RNA Granules in Germ Cells. *Cold Spring*
1103 *Harbor Perspectives in Biology* **3**. doi:10.1101/CSHPERSPECT.A002774

1104 Wang C, Yan R, Luo D, Watabe K, Liao D-F, Cao D. 2009. Aldo-keto Reductase Family 1 Member
1105 B10 Promotes Cell Survival by Regulating Lipid Synthesis and Eliminating Carbonyls. *The*
1106 *Journal of Biological Chemistry* **284**:26742–26748. doi:10.1074/jbc.M109.022897

1107 Wang SM, Lin HY, Chen YL, Hsu TI, Chuang JY, Kao TJ, Ko CY. 2019. CCAAT/enhancer-binding
1108 protein delta regulates the stemness of glioma stem-like cells through activating PDGFA
1109 expression upon inflammatory stimulation. *Journal of Neuroinflammation* **16**:1–12.
1110 doi:10.1186/S12974-019-1535-Z/FIGURES/6

1111 White M, Amino R, Mueller I. 2017. Theoretical Implications of a Pre-Erythrocytic Plasmodium vivax
1112 Vaccine for Preventing Relapses. *Trends in Parasitology* **33**:260. doi:10.1016/J.PT.2016.12.011

1113 White MT, Walker P, Karl S, Hetzel MW, Freeman T, Waltmann A, Laman M, Robinson LJ, Ghani A,
1114 Mueller I. 2018. Mathematical modelling of the impact of expanding levels of malaria control
1115 interventions on Plasmodium vivax. *Nature Communications 2018 9:1* **9**:1–10.
1116 doi:10.1038/s41467-018-05860-8

1117 White NJ. 2011. Determinants of relapse periodicity in Plasmodium vivax malaria. *Malaria Journal*
1118 **10**:297. doi:10.1186/1475-2875-10-297

1119 World Health Organization. 2021. World malaria report 2021. *World malaria report 2021*.
1120 https://www.who.int/publications/i/item/9789240040496

1121 Yokomizo T, Izumi T, Takahashi T, Kasamal T, Kobayashis Y, Satos F, Taketanill Y, Shimizu T. 1993.
1122 Enzymatic Inactivation the Porcine Kidney O f Leukotriene B4 by a Novel Enzyme Found in
1123 PURIFICATION AND PROPERTIES OF LEUKOTRIENE Bq 12-
1124 HYDROXYDEHYDROGENASE*. *THE JOURNAL OF BIOLOGICAL CHEMISTRY*
1125 **268**:18128–18135. doi:10.1016/S0021-9258(17)46820-7

1126 Youn JY, Dyakov BJA, Zhang J, Knight JDR, Vernon RM, Forman-Kay JD, Gingras AC. 2019.
1127 Properties of Stress Granule and P-Body Proteomes. *Molecular Cell* **76**:286–294.
1128 doi:10.1016/J.MOLCEL.2019.09.014/ATTACHMENT/C072E42B-EF83-4FFF-8FDE-
1129 52AB4D2E092F/MMC4.DOCX

1130 Zheng GXY, Terry JM, Belgrader P, Ryvkin P, Bent ZW, Wilson R, Ziraldo SB, Wheeler TD,
1131 McDermott GP, Zhu J, Gregory MT, Shuga J, Montesclaros L, Underwood JG, Masquelier DA,
1132 Nishimura SY, Schnall-Levin M, Wyatt PW, Hindson CM, Bharadwaj R, Wong A, Ness KD,

1133 Beppu LW, Deeg HJ, McFarland C, Loeb KR, Valente WJ, Ericson NG, Stevens EA, Radich JP,
1134 Mikkelsen TS, Hindson BJ, Bielas JH. 2017. Massively parallel digital transcriptional profiling of
1135 single cells. *Nature Communications* **8**:14049. doi:10.1038/ncomms14049

1136

1137

1138 **FIGURE LEGENDS**

1139 **Figure 1. Design and validation of detection of P. vivax liver stages using high-content imaging**
1140 **and scRNA-seq.** (A) Schematic illustrating the sample preparation and data generation pipeline used to
1141 assess P. vivax liver stage infection rates and gene expression. (B) Representative high content images
1142 of primary hepatocytes infected with *P. vivax* on day 5 (left) and day 9 (right) post-infection (p.i). Images
1143 were captured from one well from a 384-well plate with a 4x objective. Inset: one field of view (white
1144 dashed box) from the same well captured with a 20x objective. Cells were stained with DAPI (blue) and
1145 *Pv*UIS4 (green). White bar represents 1mm, inset bars represent 10µm. Images are representative of
1146 replicate 1. (C) Histogram displaying the distribution of parasite growth areas fixed at day 5 or day 9
1147 post-infection (left) and net quantity of parasites and hepatocyte nuclei (right). Net infection rate is
1148 indicated for each endpoint. Growth and infection metrics are shown for both replicates.

1149 **Figure 1—figure supplement 1**
1150 **Assessment of *P. vivax* liver stages using high-content imaging.** Representative high content images
1151 of primary hepatocytes infected with *P. vivax* on day 5 (left) and day 9 (right) post-infection. Images
1152 were obtained from one well from a 384-well plate with a 4x objective. Inset: one field of view (orange
1153 box) from the same well captured with a 20x objective. Cells were stained with DAPI (blue) and *Pv*UIS4
1154 (green). White arrow: liver form assigned as a hypnozoite, yellow arrow: liver form assigned as a
1155 schizont. White bar represents 1mm, grey bar represents 200µm. Images are representative of the second
1156 biological replicate used in the study.

1157 **Figure 2. Low dimensional representation of *P. vivax* schizont and hypnozoite transcriptomes.** (A)
1158 t-SNE plots of integrated *P. vivax* liver stage scRNA-seq data faceted by parasites isolated on day 5
1159 (left) and day 9 (right) post-infection. (B) t-SNE plot of *P. vivax* liver stage data colored by parasites
1160 encoding for putative hypnozoites (C1) and schizonts (C2). (C) t-SNE plots of *P. vivax* liver stage
1161 scRNA-seq data colored by number of transcripts detected (left), UMI counts (middle), and the
1162 expression of the schizont marker, LISP2 (PVP01_0304700) (right). Scales: absolute count (left,
1163 middle), normalized expression (right).

1164 **Figure 2—figure supplement 1**
1165 **Metrics associated with *P. vivax* liver stage scRNA-seq data analyses.** (A) Number of *P. vivax* liver
1166 stage transcriptomes assessed post-cell and gene filtering. (B) Scatter plots displaying the number of
1167 genes detected versus total number of UMIs for each parasite transcriptome assessed. Red dashed
1168 vertical line (60) represents the cut-off used to filter viable from problematic (dead/dying/poorly
1169 captured) cells. (C) Number of *P. vivax* liver stage parasites assigned to cluster 1 (hypnozoites) and
1170 cluster 2 (schizonts). SZ: schizont; HZ: hypnozoite; dpi: day post-infection.

1171 **Figure 2—figure supplement 2**

1172 **Comparision of per cell metrics with other *P. vivax* scRNA-seq data.** Violin plots showing the
1173 distribution of genes detected in the current dataset, and other single-cell gene expression assessements
1174 of *P. vivax* liver stages (Mancio-Silva et al., 2022), sporozoites (Ruberto et al., 2021b), and blood-stage
1175 parasites (Sà et al., 2020). Replicates in sporozoite and blood-stage datasets represent unique 10x
1176 Genomics' scRNA-seq library preparations. Blood-stage scRNA-seq metrics were obtained after
1177 realignment of sequencing data to an updated *P. vivax* transcriptome including UTRs as performed
1178 previously (Ruberto et al., 2021b). N = number of single-cell transcriptomes assessed for each sample.
1179 Light blue dashed horizontal line: median number genes detected or UMIs in schizonts obtained in the
1180 current dataset; teal dashed horizontal line: median number genes detected or UMIs in hypnozoites
1181 obtained in the current dataset. Day denotes day post-infection.

1182 **Figure 2—source data 1**

1183 **Summary statistics and cell and gene filtering metrics for each single-cell RNA library.**

1184 **Figure 3. *P. vivax* hypnozoites have distinct transcriptomic signatures**. (A) Dot plots showing
1185 transcripts that distinguish all hypnozoites from schizonts. The size of the dot corresponds to the
1186 percentage of cells that transcript was detected per condition, colored by average expression.
1187 Differentially expressed transcripts were identified using Seurat's FindMarker function (Wilcoxon rank-
1188 sum test, Bonferroni adjusted p values < 0.01). (B) tSNE plots of liver stages colored by transcripts
1189 displaying greater levels in hypnozoites. Colored boxes in A and B indicate the family or canonical
1190 biological process that the transcript is associated with. Scale: normalized expression; pct. exp: percent
1191 of cells expressing transcript. (C) Number of transcripts in schizonts and hypnozoites identified as
1192 cellular fating RBPs (left) and GO term enrichment of this subset (right). Adj P: Bonferroni adjusted p
1193 value.

1194 **Figure 3—figure supplement 1**

1195 ***P. vivax* schizonts and hypnozoites have distinct transcriptomic signatures.** (A) Scatterplot showing
1196 average $\log_2$ fold change versus the difference in the proportion of cells the transcript is detected in
1197 clusters encoding for hypnozoites and schizonts. Negative values: greater detection in hypnozoites;
1198 positive values: greater detection in schizonts. (B) Violin plots displaying the expression of genes
1199 encoding for TCA- and glycolysis-related proteins. (C) Dot plots showing transcripts with decreased
1200 expression in hypnozoites relative to schizonts. The size of the dot corresponds to the percentage of cells
1201 expressing the gene, colored by average expression. Differentially expressed transcripts were identified
1202 using Seurat's FindMarkers function. Wilcoxon rank-sum test, Bonferroni adjusted p values < 0.01.
1203 Scale: normalized expression; pct. exp: percent of cells expressing the gene. ldh: L-lactate

1204 dehydrogenase; gapdh: glyceraldehyde 3-phosphate dehydrogenase; atp-synthC: ATP synthase subunit
1205 C; gdh1: NADP-specific glutamate dehydrogenase 1.

1206 **Figure 3—figure supplement 2**
1207 **Carfilzomib inhibits *P. vivax* schizonts and hypnozoites.** (A) Violin plots displaying the distribution
1208 of expression of select genes encoding for proteasome subunits in schizonts and hypnozoites. (B) Table
1209 of proteasome-associated transcripts differentially expressed between schizonts and hypnozoites.
1210 Positive average log2FC: higher expression in schizonts. (C) Structure of carfilzomib. (D) Dose-
1211 response curve of carfilzomib-induced inhibition of *P. vivax* schizont growth area (yellow, IC50
1212 288nM), hypnozoite quantity per well (blue, IC_{50} 511nM), and hepatocyte nuclei quantity (orange, IC_{50}
1213 3.32 μM). Data shown are pooled from three independent experiments, each containing duplicate wells
1214 at each concentration. Bars represent ± SEM.

1215 **Figure 3—source data 1**
1216 **Data associated with schizonts versus hypnozoites analyses.** (A) Differentially expressed genes
1217 defining schizonts and hypnozoites. Positive Average log 2 FC: Upregulated in hypnozoites relative to
1218 schizonts. Rows highlighted in yellow denote inclusion cutoffs for genes considered differentially
1219 expressed (Bonferroni adjusted p value < 0.01 & absolute (average log2 fold change [FC]) > 0.5). (B)
1220 Differentially expressed genes identified as encoding for cellular fating RNA-binding proteins. (C) GO
1221 Term enrichment of Hypnozoite or Schizont transcripts identified as cellular fating RBPs. Rows
1222 highlighted in light green are terms with Bonferroni adjusted p value < 0.05. Input parameters: P value
1223 cutoff = 0.05; Limit to GO Slim terms = No; Evidence: Computed, curated; PlasmoDB v55.

1224 **Figure 4. Transcriptomic signatures of activating and persister hypnozoites.** (A) Number of
1225 hypnozoites assessed (left) and UMAP of cells identified as hypnozoites colored by day of collection.
1226 (B) Proportion of cells in clusters on days 5 and 9 post-infection (left) and UMAP of hypnozoites colored
1227 by cluster. (C) Violin plot showing the expression of LISP2 in each cluster. (D) Dot plot showing
1228 markers that distinguish hypnozoites in each cluster. The size of the dot corresponds the percentage of
1229 cells in the expressing the gene of interest, colored by scaled normalized expression of the transcript in
1230 each cluster. Marker transcripts were identified using Seurat's AllFindMarkers function. Wilcoxon
1231 rank-sum test, average $log_2FC > 1$, Bonferroni adjusted p value < 0.01. (E) Number transcripts in each
1232 cluster encoding for cellular fating RBPs sorted by their average log2FC relative to the other clusters
1233 (top) and GO Term enrichment of genes in each cluster (bottom). Adj P: Bonferroni adjusted p value.

1234 **Figure 4—supplement 1**
1235 **Assessment of hypnozoite transcriptomes.** (A) UMAP of hypnozoites colored by cluster and faceted
1236 by day post-infection. (B) Violin plot showing the average log_2FC of differentially expressed genes in

1237 each cluster. Markers were identified using Seurat's AllFindMarkers function. Genes with an Bonferroni
1238 adjusted p value < 0.05 (Wilcoxon rank-sum) and average log_2FC > 0.5 were deemed markers. Red
1239 dashed line: average log_2FC = 0.5.

1240 **Figure 4—source data 1**
1241 **Data associated with analyses of hypnozoite-to-hypnozoite heterogeneity.** (A) Markers defining
1242 each hypnozoite cluster. Marker defined as: Average log 2 FC > 0.5, Adjusted p value < 0.05. Rows
1243 colored green are transcripts that meet marker criteria. (B) Differentially expressed genes identified as
1244 encoding for cellular fating RNA-binding proteins in hypnozoite clusters. (C) GO Term enrichment of
1245 hypnozoite transcripts identified as cellular fating RBPs. Rows highlighted in light green are terms with
1246 Bonferroni adjusted p value < 0.05. P value cutoff = 0.05; Limit to GO Slim terms = No; Evidence:
1247 Computed, curated; PlasmoDB v55.

1248 **Figure 5. Analysis of host-pathogen transcriptional signatures in *P. vivax*- infected and non-**
1249 **infected hepatocytes.** t-SNE plots of hepatocytes faceted by infection status. Grey, noninfected (naive
1250 and exposed) hepatocytes; light blue, hepatocytes infected with schizonts; teal, hepatocytes infected
1251 with hypnozoites.

1252 **Figure 5—supplement 1**
1253 **Analysis of host-pathogen transcriptional signatures in *P. vivax*- infected and non-infected**
1254 **hepatocytes.** (A) Number of hepatocytes assessed. Colored by infection status and faceted by sample
1255 (left); proportion of infected, exposed, or naive hepatocytes assessed on day 5 or day 9 post-infection.
1256 (B) t-SNE plot of hepatocytes colored by day. (C) t-SNE plots of hepatocytes colored by percent
1257 expression of zonation markers in human hepatocytes. Markers obtained from Macparland et al. (2019).
1258 (D) t-SNE plots of hepatocytes colored by hypnozoite infection status. Grey, uninfected (naive and
1259 exposed) hepatocytes; red, hepatocytes infected with C1 hypnozoites; blue, hepatocytes infected with
1260 C2; teal, hepatocytes infected with C3 hypnozoites. (E) Unique and overlapping gene sets in hepatocytes
1261 infected with schizonts or hypnozoites. Positive enrichment derived from genes displaying greater
1262 expression versus non-infected hepatocytes; negative enrichment derived from transcripts displaying
1263 decreased expression versus noninfected hepatocytes.

1264 **Figure 6. Analysis of host transcriptional signatures in *P. vivax* infected hepatocytes.** (A) Volcano
1265 plots showing changes in gene expression in infected hepatocytes versus non infected (Wilcoxon rank
1266 sum, Bonferroni adjusted p value < 0.05). Positive fold change (FC) values represent genes with greater
1267 expression, and negative FC values represent genes with decreased expression. Dashed horizontal red
1268 lines: Bonferroni adjusted p value = 0.05; dashed vertical red lines: log_2FC = 0.5. (B) Summary of
1269 differential gene expression data shown in the volcano plots and of the enrichment analyses. Hep:

1270 hepatocyte. (C) Enrichment map of cellular processes and pathways associated with hepatocyte infection
1271 with *P. vivax* schizonts. (D) Enrichment map of cellular processes and pathways associated with
1272 hepatocyte infection with *P. vivax* hypnozoites. For the maps depicted in panels C and D, node size is
1273 proportional to the number of genes identified in each gene set (minimum 3 genes/gene set); each node
1274 represents a distinct biological process or pathway derived from gene with decreased expression (red)
1275 or increased expression (blue) versus non-infected cells; and edges (blue lines) represent the number of
1276 genes overlapping between two processes or pathways. (E) Representative confocal image of *P. vivax*
1277 parasites on day 12 post-infection of hepatocytes (left). Cells were stained with DAPI (blue), *Pv*UIS4
1278 (green), and *Hs*AKR1B10 (red). White bar represents 100µm. Violin plot displaying the distribution of
1279 AKR1B10 signal in hepatocyte cultures infected with *P. vivax* (right). SZ: hepatocyte containing
1280 schizont; HZ: hepatocyte containing hypnozoite; EX: hepatocyte not infected but exposed to *P. vivax.*
1281 ****: p <= 0.0001.

1282 **Figure 6—figure supplement 1**
1283 **Human AKR1B10 is upregulated in hepatocytes infected with *P. vivax*.** (A) Violin plots displaying
1284 the distribution of *AKR1B10* transcript levels in infected (schizonts and hypnozoites) and non-infected
1285 (exposed and naive) hepatocytes. Black dot: mean expression (log_2). Adj p: Bonferroni adjusted p value
1286 versus non-infected (naïve and exposed) hepatocytes. (B) Representative confocal image from a second
1287 biological replicate of *P. vivax* parasites on day 12 post-infection of hepatocytes. Cells were stained with
1288 DAPI (blue), *Pv*UIS4 (green), and *Hs*AKR1B10 (red). White bar represents 100µm.
1289 (D) Associated with **Figure 6E** (right), violins plots displaying the distribution of AKR1B10 signal
1290 across all biological replicates. IFA: immunofluorescence assay; SZ: hepatocyte containing schizont;
1291 HZ: hepatocyte containing hypnozoite; EX: hepatocyte not infected but exposed to *P. vivax.* ****: p <=
1292 0.0001; *: p <= 0.05; n.s: not significant, p > 0.05.

1293 **Figure 6—source data 1**
1294 **Data associated with host-specific transcriptional signatures in response to *P. vivax* infection.** (A)
1295 Differentially expressed genes in hepatocytes containing schizonts versus non-infected cells. Positive
1296 average log2FC: greater expression in infected hepatocytes. (B) Differentially expressed genes in
1297 hepatocytes containing hypnozoites versus non-infected cells. Positive average log2FC: greater
1298 expression in infected hepatocytes. (C) Enrichment of GO biological processes and Reactome metabolic
1299 pathways. (D) Unique and overlapping enriched gene sets in hepatocytes infected with schizonts or
1300 hypnozoites. (E) Differentially expressed genes in non-infected hepatocytes exposed to *P. vivax*
1301 (exposed) versus non-infected hepatocytes never exposed to *P. vivax* (naïve). Postive average log2FC:
1302 greater expression in non-infected hepatocytes exposed to *P. vivax* (exposed). Seurat FindMarkers
1303 parameters used to generate gene list: logfc.threshold = 0.25, min.pct = 0.25, only.pos = F,
1304 max.cells.per.ident = 20731, assay = "RNA". (F) Enrichment of GO biological processes and

1305 REACTOME metabolic pathways that are downregulated in non-infected hepatocytes exposed to *P.*
1306 *vivax* (exposed) versus non-infected hepatocytes never exposed to *P. vivax* (naïve). Genes in **Figure 6—**
1307 **source data 1E** highlighted in green were used as input to generate enrichment lists.

1308 **Figure 7. Transcription factor enrichment in hepatocytes infected with schizonts or hypnozoites.**
1309 Dot plot of transcription factors enriched in Hepatocyte$^{+hypnozoite}$ (left) or Hepatocyte$^{+schizont}$ sets (right).
1310 Positive (+) enrichment derived from genes displaying greater expression versus non-infected
1311 hepatocytes; negative (-) enrichment derived from genes displaying decreased expression versus
1312 noninfected hepatocytes.

1313 **Figure 7—source data 1**
1314 **Transcription factor enrichment analysis.** Rows highlighted in green are sets that are significantly
1315 enriched, adjusted p value < 0.05.

Figure 1

A

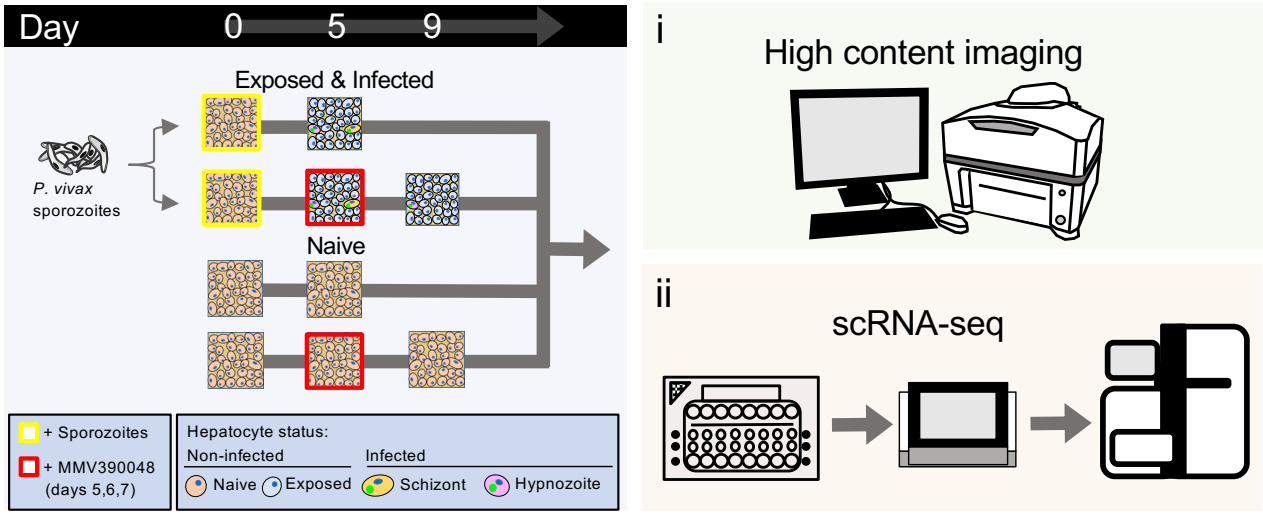
Day
0
5
9
Exposed & Infected
P. vivax
sporozoites
Naive
+ Sporozoites
+ MMV390048
(days 5,6,7)
Hepatocyte status:
Non-infected
Infected
Naive
Exposed
Schizont
Hypnozoite
i
High content imaging
ii
scRNA-seq

B

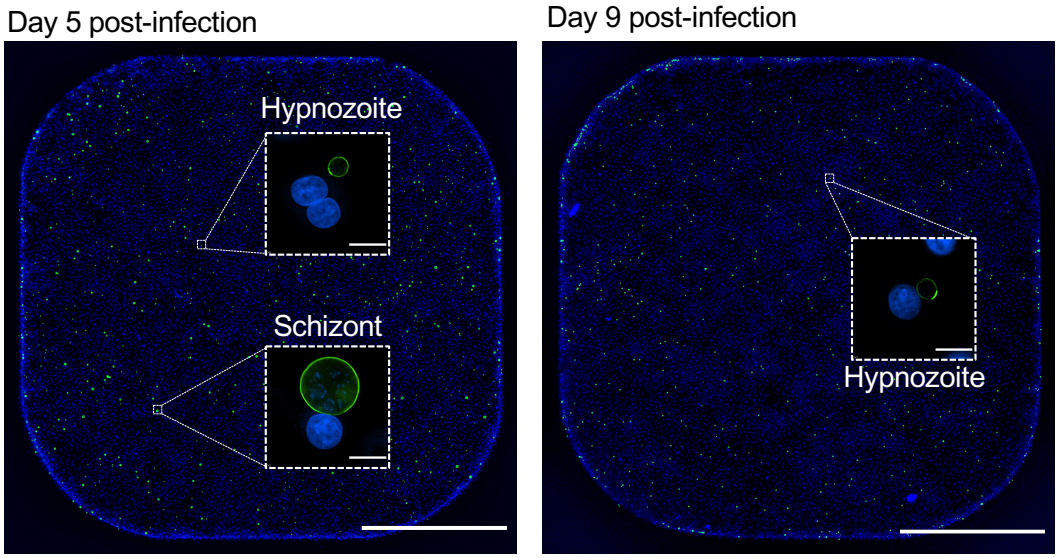
Day 5 post-infection
Day 9 post-infection
Hypnozoite
Schizont
Hypnozoite

C

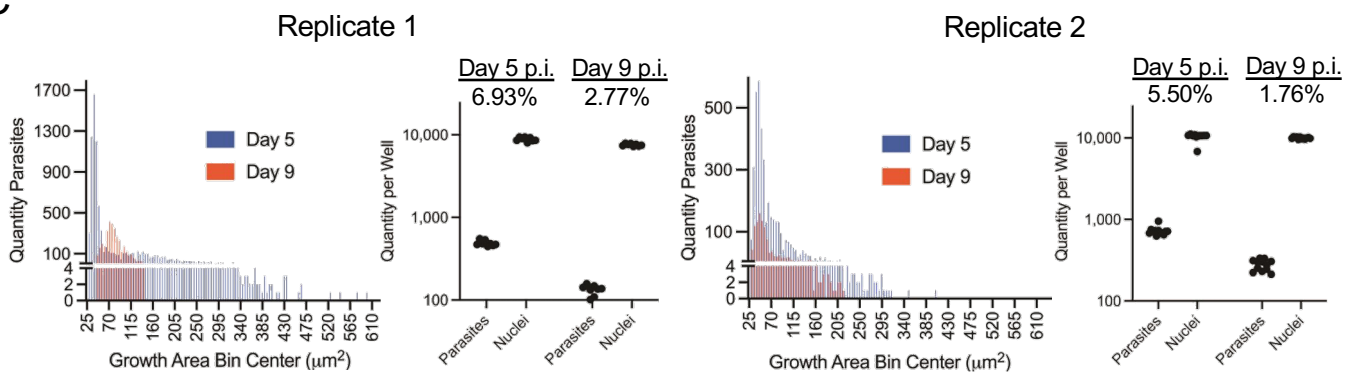
Replicate 1
Replicate 2
Quantity Parasites
Day 5
Day 9
Growth Area Bin Center (μm²)
Quantity per Well
Day 5 p.i.
Day 9 p.i.
6.93%
2.77%
5.50%
1.76%
Parasites
Nuclei

Figure 2

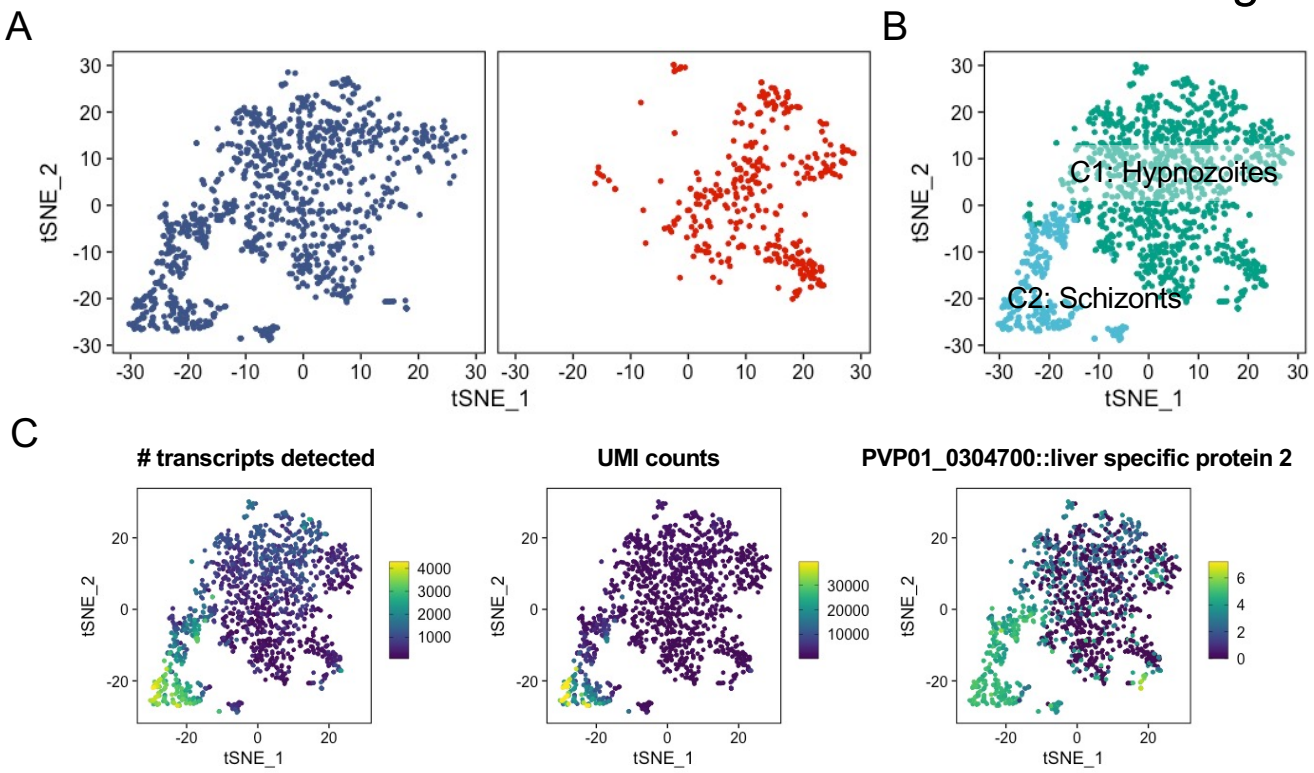
A
B
C
tSNE_1
tSNE_2
C1: Hypnozoites
C2: Schizonts
transcripts detected
UMI counts
PVP01_0304700::liver specific protein 2

Figure 3

A

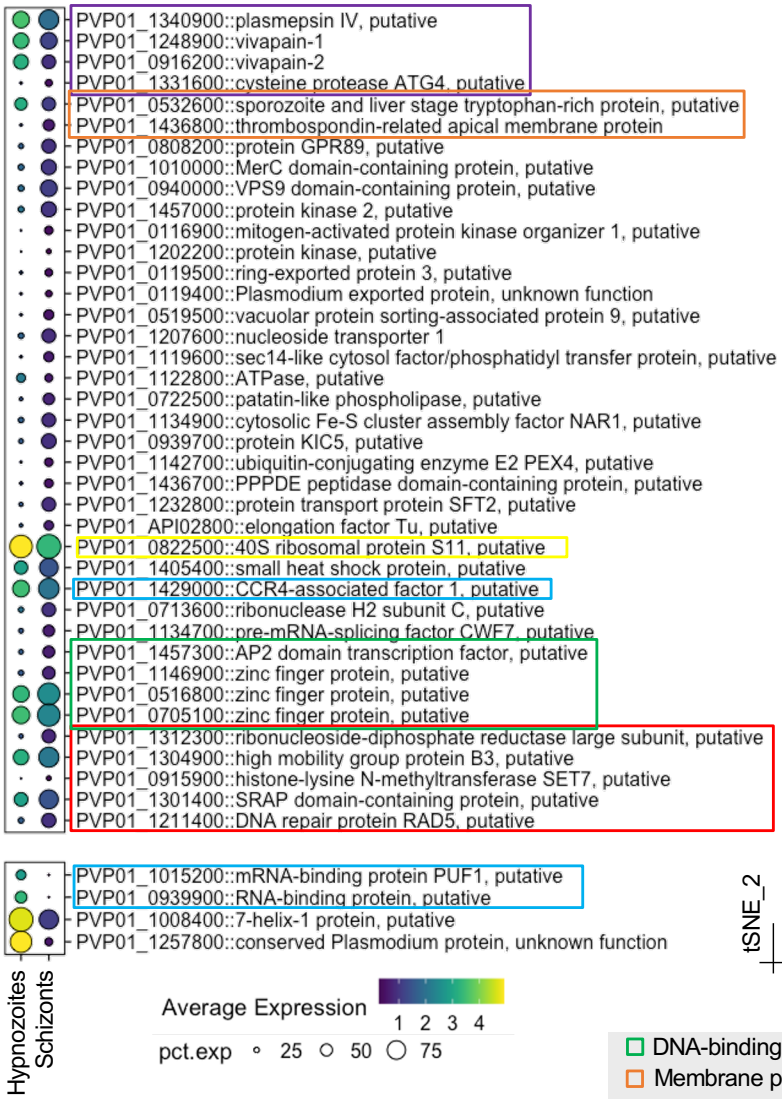

B

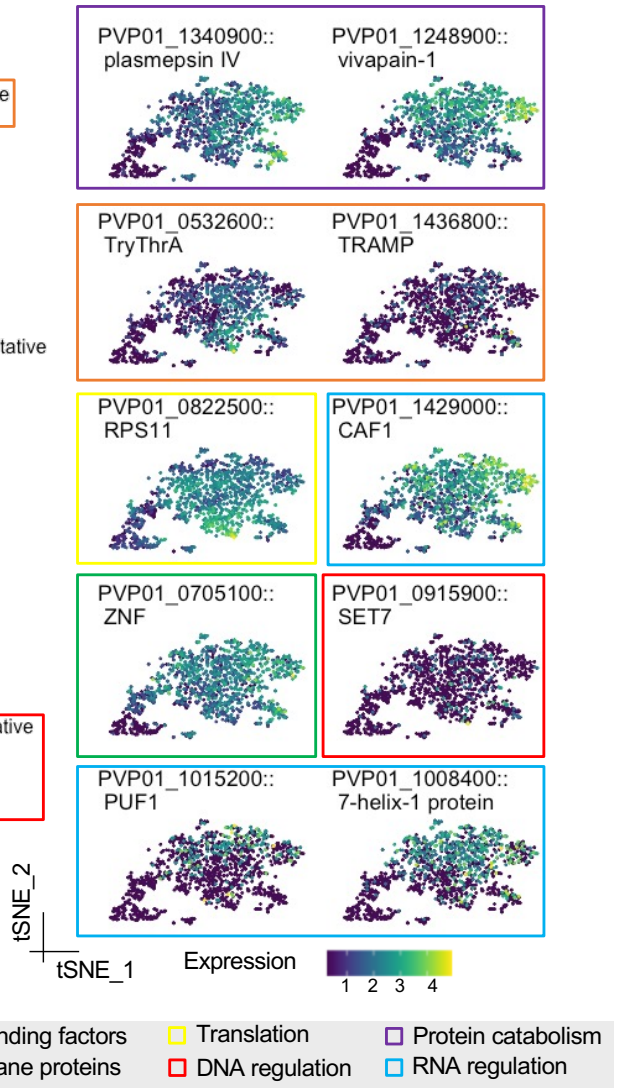

C

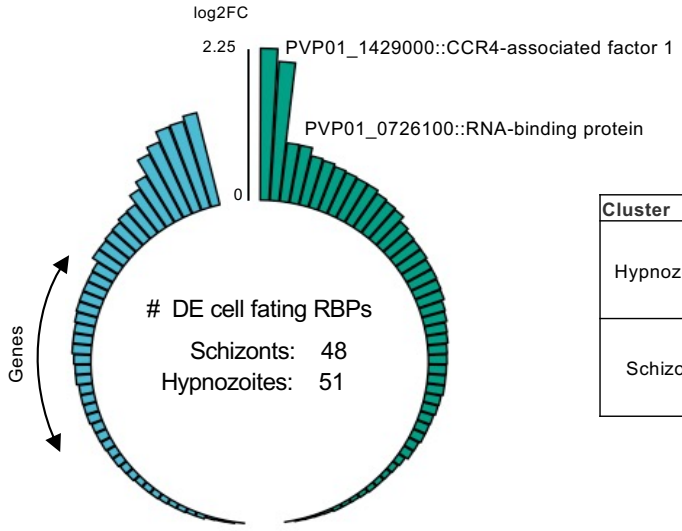

Cluster	GO Term	Adj P
Hypnozoites	CCR4-NOT complex	2.20e-9
	Nucleus	1.22e-2
	P body	2.28e-2
	Regulation of gene expression	1.97e-6
Schizonts	Eukaryotic translation initiation factor 3 complex	5.22e-6
	RNP complex	2.35e-5
	Translation preinitiation complex	1.46e-4
	Translation	7.83e-7

Figure 4

A

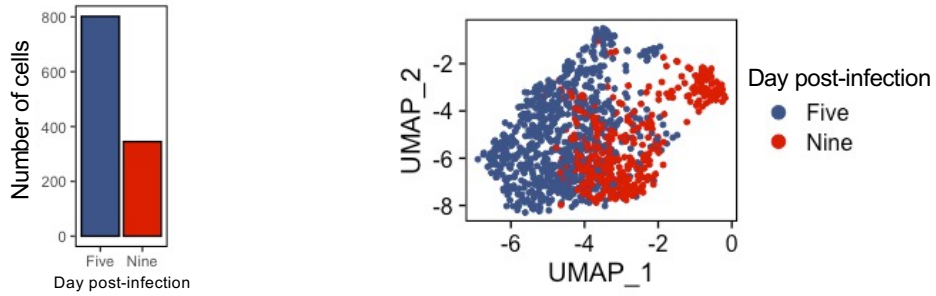

B

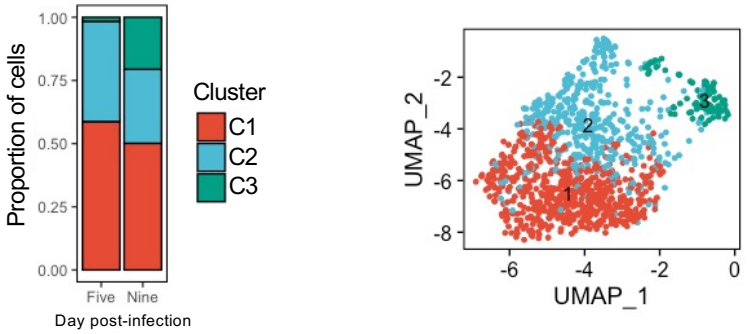

C

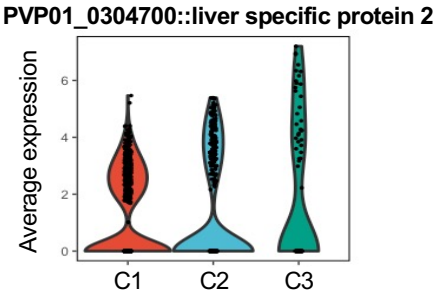

D

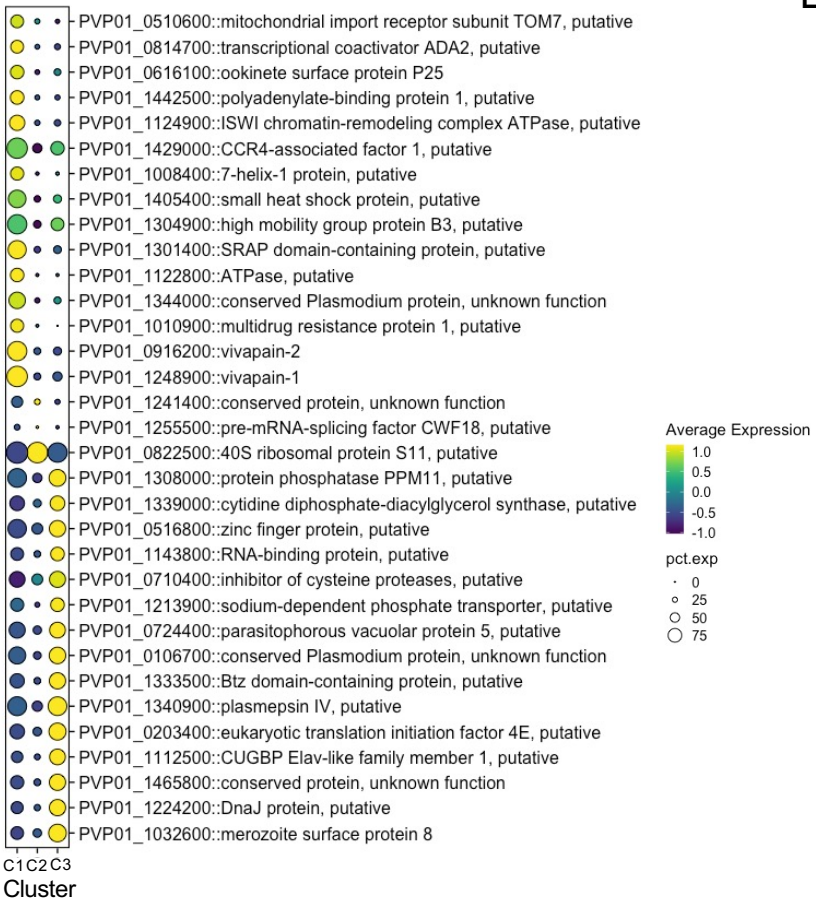

E

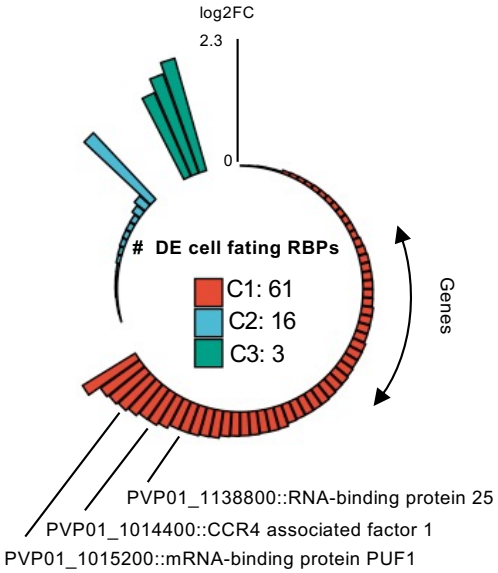

Cluster	GO Term	Adj P
C1	CCR4-NOT complex	1.15e-04
	Germ plasm	2.62e-03
	P granule	2.62e-03
C2	Regulation of RNA splicing	5.05e-05
	Ribonucleoprotein complex	3.54e-04
	Translation	4.83e-02
C3	Translational initiation	5.36e-02
	RNA binding	3.01e-03
	Nucleic acid binding	6.71e-03

Figure 5

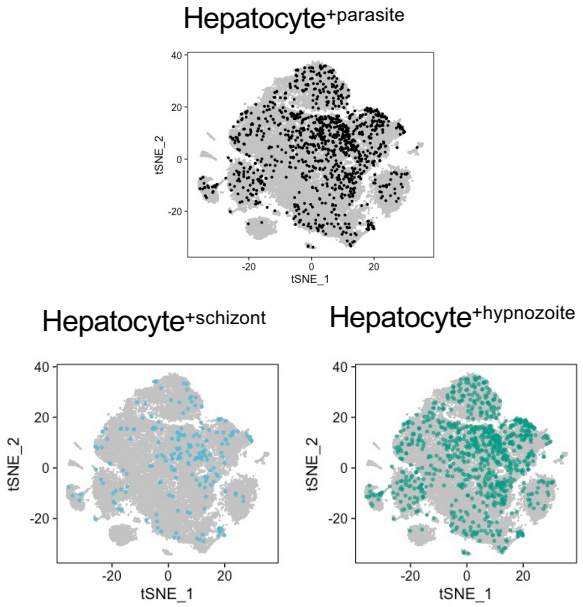
Hepatocyte+parasite
Hepatocyte+schizont
Hepatocyte+hypnozoite
tSNE_1
tSNE_2
40
20
0
-20

Figure 6

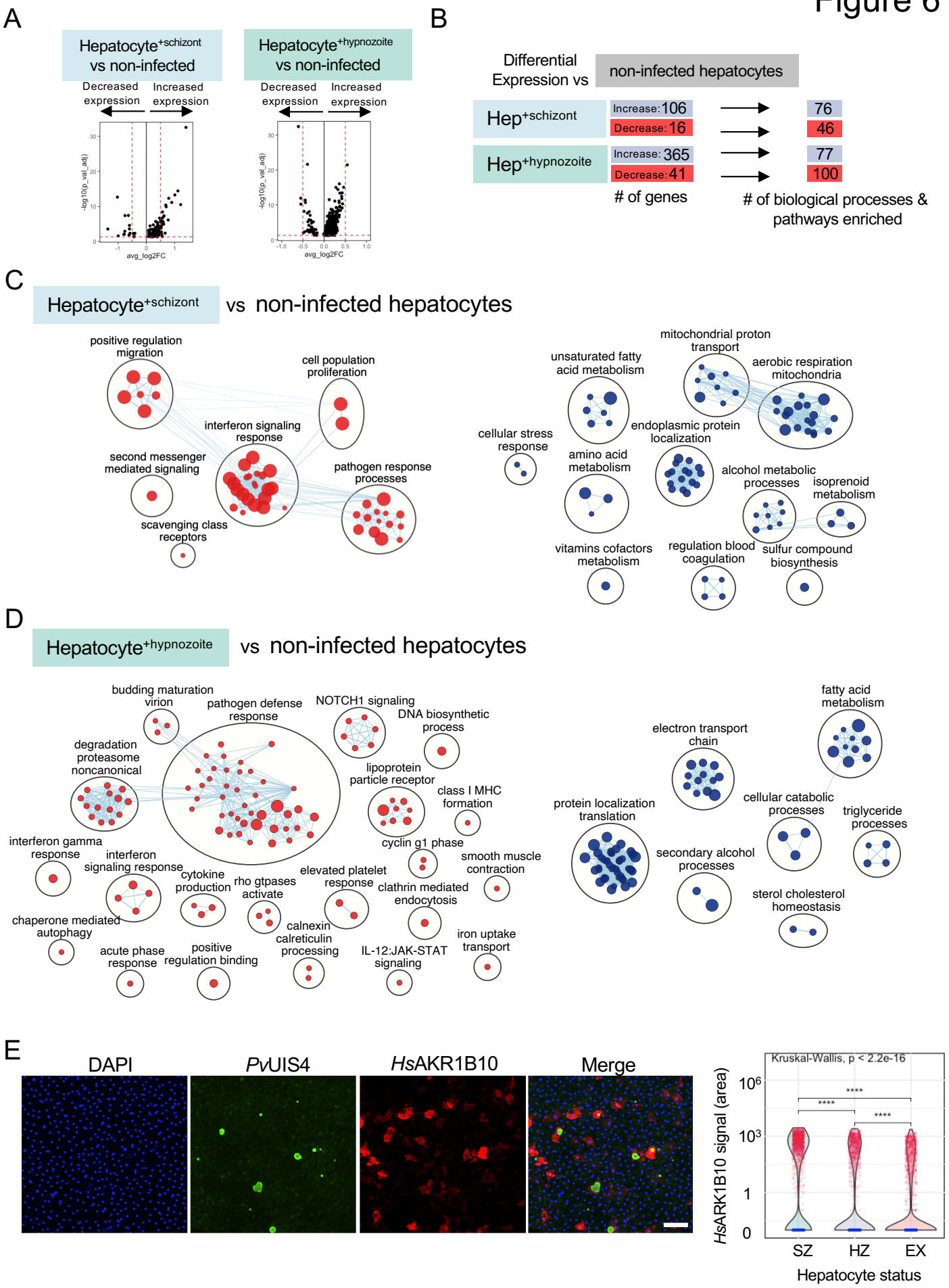
A
Hepatocyte+schizont vs non-infected
Hepatocyte+hypnozoite vs non-infected
Decreased expression
Increased expression
-log10(p_val_adj)
avg_log2FC
B
Differential Expression vs
non-infected hepatocytes
Hep+schizont
Increase: 106
Decrease: 16
76
46
Hep+hypnozoite
Increase: 365
Decrease: 41
77
100
# of genes
# of biological processes & pathways enriched
C
Hepatocyte+schizont vs non-infected hepatocytes
positive regulation migration
cell population proliferation
interferon signaling response
second messenger mediated signaling
pathogen response processes
scavenging class receptors
mitochondrial proton transport
unsaturated fatty acid metabolism
aerobic respiration mitochondria
cellular stress response
endoplasmic protein localization
amino acid metabolism
alcohol metabolic processes
isoprenoid metabolism
vitamins cofactors metabolism
regulation blood coagulation
sulfur compound biosynthesis
D
Hepatocyte+hypnozoite vs non-infected hepatocytes
budding maturation virion
pathogen defense response
NOTCH1 signaling
DNA biosynthetic process
degradation proteasome noncanonical
lipoprotein particle receptor
class I MHC formation
interferon gamma response
interferon signaling response
cyclin g1 phase
smooth muscle contraction
cytokine production
rho gtpases activate
elevated platelet response
clathrin mediated endocytosis
chaperone mediated autophagy
calnexin calreticulin processing
iron uptake transport
acute phase response
positive regulation binding
IL-12:JAK-STAT signaling
fatty acid metabolism
electron transport chain
protein localization translation
cellular catabolic processes
triglyceride processes
secondary alcohol processes
sterol cholesterol homeostasis
E
DAPI
PvUIS4
HsAKR1B10
Merge
Kruskal-Wallis, p < 2.2e-16
HsARK1B10 signal (area)
SZ
HZ
EX
Hepatocyte status

Figure 7

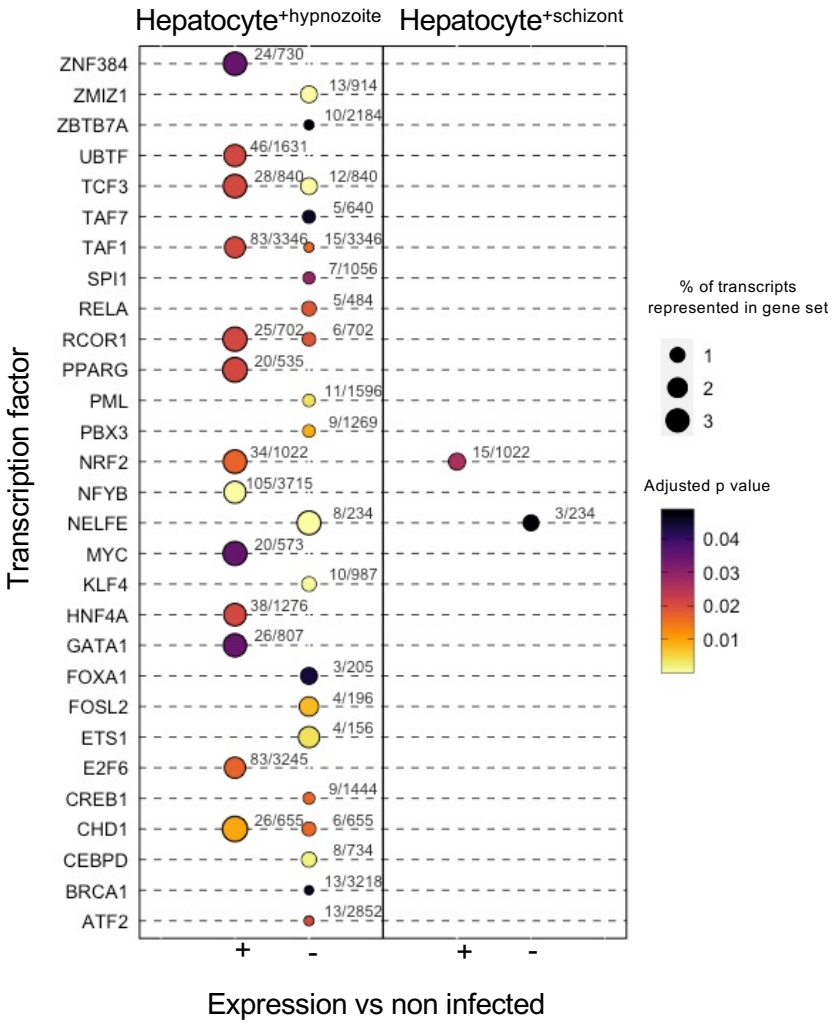
Hepatocyte+hypnozoite
Hepatocyte+schizont
Transcription factor
ZNF384
ZMIZ1
ZBTB7A
UBTF
TCF3
TAF7
TAF1
SPI1
RELA
RCOR1
PPARG
PML
PBX3
NRF2
NFYB
NELFE
MYC
KLF4
HNF4A
GATA1
FOXA1
FOSL2
ETS1
E2F6
CREB1
CHD1
CEBPD
BRCA1
ATF2
24/730
13/914
10/2184
46/1631
28/840
12/840
5/640
83/3346
15/3346
7/1056
5/484
25/702
6/702
20/535
11/1596
9/1269
34/1022
15/1022
105/3715
8/234
3/234
20/573
10/987
38/1276
26/807
3/205
4/196
4/156
83/3245
9/1444
26/655
6/655
8/734
13/3218
13/2852
+
-
+
-
Expression vs non infected
% of transcripts represented in gene set
1
2
3
Adjusted p value
0.04
0.03
0.02
0.01